A parametric investigation on applicability of the curved shell finite element model to nonlinear response prediction of planar RC walls

Farhad Dashti[1]; Rajesh P Dhakal[2]; and Stefano Pampanin[3]

Abstract This study investigates the ability of a finite element model based on curved shell element formulation in predicting nonlinear behavior of planar RC structural walls, identifying the strengths and limitations of this modeling approach. For this purpose, a parametric validation is conducted in addition to verification of the model simulation against experimental results of several wall specimens tested in literature. The effects of variations in total length, thickness, shear-span ratio, axial load ratio, confinement, as well as the horizontal and vertical reinforcement ratios are investigated at both global and local levels. For scrutinizing the global response, lateral load versus total, flexural and shear deformation predictions are used. For local response, sensitivity of the stress and strain distributions throughout the length and height of the wall models to the parameters noted above is evaluated. The capabilities and deficiencies of the modelling approach are discussed in detail in light of the numerical vs experimental as well as parametric verifications. The model is found to be able to predict most of the experimentally observed failure mechanisms of rectangular walls including global out-of-plane instability under in-plane loading, concrete crushing at the base, diagonal tension and diagonal compression as well as sliding shear. The model is not able to represent bar buckling, bar fracture and the potential subsequent secondary failure modes such as instability of the compression boundary zone due to progressive asymmetric concrete crushing at the base. The parametric study indicated sensitivity of the model response to the variation of the parameters known to be influential on the nonlinear response of planar RC walls.

Keywords Reinforced concrete walls, Failure mechanisms, Numerical prediction, Parametric study

1. Introduction

The performance of structural walls in the several major earthquakes during the last ten years has raised concerns on the current understanding of the seismic response of these key structural components. Several failure patterns were observed in structural walls in these earthquakes such as buckling of bars, crushing/spalling of concrete, out-of-plane deformation also referred to as lateral instability (especially involving the part of the wall length that had deteriorated in compression in previous cycles), longitudinal reinforcement failing in tension and being hidden behind a single small residual crack, etc. Some of these failures are attributable to deficiencies of the associated design provisions such as the requirements for confinement in the boundary element or for buckling restraint detailing. However, some of the failures are not yet fully understood. In some cases, lateral instability (global buckling) of a large portion of a wall section was observed. Prior to the Chile and Canterbury earthquakes, this global buckling failure had only been primarily observed in laboratory tests (Beattie 2004; Goodsir 1985; Johnson 2010; Oesterle et al. 1976; Thomsen IV and Wallace 1995; Vallenas et al. 1979).

Several research projects have been/are being conducted on different failure mechanisms of different types of structural walls using analytical, numerical and experimental approaches (Alarcon et al. 2014; Almeida et al. 2017; Brueggen et al. 2017; Dashti et al. 2017; Dashti et al. 2018a; Fischinger et al. 2017; Haro et al. 2018; Herrick and Kowalsky 2016; Kolozvari and Wallace 2016; Lu et al. 2016; Parra and Moehle 2017; Rosso et al. 2015;

---

[1] Post-doctoral Research Engineer, UC Quake Centre, Department of Civil and Natural Resources Engineering, Univ. of Canterbury, Christchurch 8140, New Zealand. E-mail: farhad.dashti@canterbury.ac.nz

[2] Professor, Department of Civil and Natural Resources Engineering, Univ. of Canterbury, Christchurch 8140, New Zealand. E-mail: rajesh.dhakal@canterbury.ac.nz

[3] Professor, Department of Structural and Geotechnical Engineering, Sapienza University of Rome, Italy. E-mail:stefano.pampanin@uniroma1.it

Rosso et al. 2017a; Sanada et al. 2017; Shegay et al. 2018; Tarquini et al. 2017; Terzioglu et al. 2018; Welt et al. 2016). Despite significant advances in the numerical solution methods and the availability of high-speed computing machines, simulation of all the failure mechanisms observed in reinforced concrete structures is still a complex task. On the other hand, size restrictions of the laboratories as well as limitations of the loading facilities put limits on the dimensions of the test specimens. With the prototype models designed taking these restrictions into account, dimensions of the wall specimens (particularly wall length) are remarkably smaller than the ones designed and constructed in real practice. Therefore, the numerical prediction is still considered as an alternative for investigating the seismic response of structural walls.

Dashti et al. (2014a, 2014b) proposed a numerical modeling technique using curved shell elements available in DIANA commercial program for numerical modeling of structural walls. The model could reasonably simulate nonlinear response of structural walls and predict the out-of-plane deformation that was observed in several rectangular wall specimens under in-plane loading. Parra (2016) used this modeling approach to investigate the out-of-plane response of wall units and the corresponding boundary zones. Rosso et al. (2017b) simulated the response of thin RC columns prone to out-of-plane instability using this method. Scolari (2017) compared the out-of-plane response captured by PARC_CL 2.0 crack model with the one predicted by this model. A validation of the model was conducted by Dashti (2017) and Dashti et al. (2017, 2018b, 2018c) which mainly focused on verification of the out-of-plane instability simulated by the model using results of several tested wall specimens as well as a blind prediction practice. The response of several wall specimens that exhibited various failure mechanisms in the laboratory were simulated by several modeling approaches within the modeling group of the Virtual International Institute for Performance Assessment of Structural Wall (NSF SAVI Wall Institute). Different macroscopic and finite element model formulations were validated against these specimens that reflected a broad range of wall configurations and response characteristics (Kolozvari et al. 2018, 2019). One of the numerical (FEM) modeling techniques involved using curved shell elements available in DIANA commercial program. However, not all the features of wall response used for the verification practice could be included in Kolozvari et al. (2019) and further details on strengths and limitations of this modeling approach are presented in this study.

Although the model based on curved shell element formulation was verified by Dashti et al. (2017) against test results of wall specimens with different failure mechanisms, the investigation was limited to prediction of mainly the global response parameters. In this paper, in addition to some of the previously verified response parameters (such as the load vs total top displacement curves), an extensive validation is conducted on the local response parameters (such as distribution of shear and flexural displacement profiles along the wall height). Also, the accuracy of the model in predicting the shear and flexural hysteretic response and their reflection on the global load-displacement hysteretic curves are elaborated. Furthermore, the simulation practice conducted using this method is extended to parametric investigations on the observed failure patterns. For this purpose, sensitivity of the wall models to a set of parameters known to be influential on evolution of different failure mechanisms in structural walls is investigated. The correlation of shear-span ratio, confinement length, longitudinal and horizontal reinforcement ratios, axial load ratio as well as wall dimensions with some of the response characteristics of structural walls is investigated. These response features include the contribution of shear and flexural displacement components to the total top displacement at different stages of loading, strain gradients along the length and height of the wall, principal stress and strain distributions, axial growth and out-of-plane response. It should be mentioned that as this parametric study is conducted to evaluate the sensitivity of the model to variation of the parameters that logically influence nonlinear response and failure pattern of structural walls, a limited range of variation is considered. However, since the model has been verified using experimental results of walls with different failure mechanisms, the parametric analysis also represents the likely behavior of walls with the characteristics of the parametric models. Hence, the results will be valuable in understanding how failure modes of RC walls change with alteration of key design parameters.

2. Numerical model

The quadrilateral four-node curved shell element (Q20SH) available in the commercial finite element analysis software DIANA (DIANA, 2011; Figure 1a) is used in this study to simulate nonlinear behavior of the considered RC wall specimens. The model element is characterized by three translational and two rotational degrees of freedom (DOFs) at each element node (no drilling DOF); the polynomials for the translations u and the rotations ϕ are expressed in Figure 1a. The element formulation uses linear interpolation with four (2×2) Gauss integration points over the element area, while the integration over the element thickness is performed using three integration points (one point in the element reference plane and two points in outer wall fibers, Figure 1b) with Simpson

2

integration scheme. Therefore, the element is capable of capturing deformations in both in-plane and out-of-plane directions.

The in-plane behavior of the concrete material within the four-node element used is governed by the *Total Strain Crack Model* available in DIANA (2011). The material model, derived from the Modified Compression Field Theory (Vecchio and Collins 1986), treats strains and stresses in the average sense to obtain the fracture energy within the element, and allows the use of two available crack models: 1) the fixed orthogonal crack model, in which the orientation of the crack is fixed during the entire computational process, and 2) the coaxial rotating crack model, in which the orientation of cracks rotates with the axes of principal strains. The fixed crack model requires definition of explicit constitutive shear strain-stress relationship, involving additional ad-hoc modeling parameters that require calibration, which could be considered as a shortcoming of the fixed-crack model. In contrast, in the rotating crack model, the shear stiffness is associated with the rotation of the material principal axes (cracks), and therefore does not require specification and validation of the shear-related modeling parameters. However, the rotating crack assumption and the assumption that the principal stresses and strains remain coaligned during the analysis are limitations of the rotating crack model since they do not represent the physical behavior of concrete. Given the advantages and disadvantages of both crack models, the rotating crack model is used in this study to represent the nonlinear behavior of concrete in the wall model.
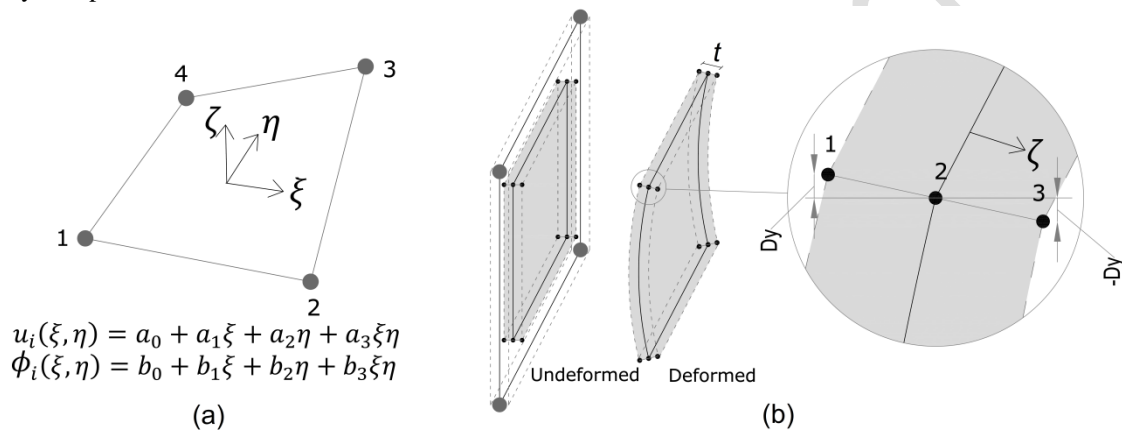

$$u_i(\xi, \eta) = a_0 + a_1\xi + a_2\eta + a_3\xi\eta$$
$$\phi_i(\xi, \eta) = b_0 + b_1\xi + b_2\eta + b_3\xi\eta$$

(a)   (b)

Figure 1. Four-node curved shell element (DIANA 2011): a) in-plane interpolation, b) three-point integration scheme over the element thickness.

The equations proposed by Chang and Mander (1994) are implemented in the Total Strain Rotating Crack model to represent the backbone behavior of confined and unconfined concrete in compression, while the tensile behavior of concrete is defined using the relations proposed by Belarbi and Hsu (1994). The cyclic concrete behavior is simulated using origin-oriented (secant) hysteretic rules. The effects of cracking and crushing on deterioration of concrete stress-strain behavior are considered using internal damage variables.

Steel reinforcement is simulated using elements that are embedded in structural elements (so-called mother elements) and do not have degrees of freedom of their own, and can be represented by single bars or layers of reinforcement. Strains in the reinforcement are computed from the displacement field of the mother elements, implying perfect bond between the reinforcement and the surrounding material. The stress-strain curve of the reinforcing steel is defined using the well-known Menegotto and Pinto (1973) model, which does not incorporate the bar buckling behavior.

The out-of-plane behavior of the four-node element is governed by a curved shell element formulation in which: 1) the in-plane lamina strains vary linearly over the element thickness, 2) transverse shear deformation is included according to the Mindlin-Reissner theory (Mindlin 1951; Reissner 1945), 3) normal to the element reference surface remains straight after deformation but not necessarily perpendicular to the reference surface, and 4) the normal stress component in the normal direction of a lamina is forced to zero. The above-described curved shell element formulation allows simulation of out-of-plane deformations under in-plane loading without making use of an artificial eccentricity.

The inputs for the Total Strain Crack model comprise of two parts: 1) basic properties like the Young's modulus, Poisson's ratio, etc., and 2) the definition of the behavior in tension, shear, and compression. Calibration of confined and unconfined concrete follows the procedure described by Orakcal and Wallace (2006). The tensile

3

and compressive behaviors are specified using the multi-linear diagram approach and with the stress-strain data calculated using the constitutive models mentioned previously.

The nonlinear analysis is conducted using the displacement control incremental procedure along with the Quasi-Newton (also called 'Secant') iterative method. The convergence tolerance has been chosen after several trials so as to generate smooth curves within the minimum analysis time possible (Force tolerance:1e-3, Energy tolerance:1e-4). Geometric nonlinearity has been accounted for in the analysis. A purely incremental method usually leads to inaccurate solutions in nonlinear analysis, unless very small step sizes are used. In an iterative process (such as the Secant method used herein) the errors that occur can be reduced successively (which in fact realizes an implicit procedure) and, therefore, the allowable step size is usually higher than in case of a process without iterations (e.g. an explicit process). However, small step sizes are chosen in this study to more accurately predict: 1) the loading step corresponding to the initial progression of out-of-plane displacement, and 2) the value of out-of-plane displacement since, considering the P-delta (also known as second-order) effects, its amount at each step depends on the initial amount.

3. Experimental verification

Table 1 provides properties of the test specimens used for validation of the model along with other modeling approaches presented in Kolozvari et al. (2019), where the numerical vs experimental comparisons are described in terms of load-displacement responses as well as the observed and predicted failure patterns. In this paper, a more comprehensive comparison of the numerical vs experimental behavior is provided using different features of the wall response.

Table 1. Experimental data for planar wall test specimens

Specimen	Scale	f'_c (MPa)	f_{yBE} (MPa)	ρ_{vBE}[1] $\rho_{h,web}$[2]/$\rho_{v,web}$[3] (%) (%)	$M/(VL_w)$[4]	$P/(A_gf_c)$[5]	$V_{max}/(A_{cv}\sqrt{f_c})$[6] (MPa)	$V_{max}/V_{nominal}$[7]	$M_{max}/M_{nominal}$[8]	Failure Mode[9]
RW2	0.33	34.0	434	2.93 0.33/0.33	3.1	0.09	0.22	0.52	1.16	CB
R2	0.33	46.4	450	4.00 0.31/0.25	2.4	0.00	0.17	0.42	1.23	OOP
WSH6	0.49	45.6	576	1.54 0.25/0.46	2.3	0.11	0.3	0.83	1.11	CB
S6	0.37	27.8	482	5.6 0.55/0.55	1.6	0.05	0.53	0.8	1.12	CB-OOP
SP4	0.5	55.8	477	6.06 0.73/0.73	1.5	0.1	0.65	0.89	1.19	DC

1) Vertical reinforcement ratio in the boundary regions; 2) Horizontal reinforcement ratio in the web region; 3)Vertical reinforcement ratio in the web region; 4) Shear-span ratio; 5) Axial load ratio; 6) Shear stress; 7) Applied shear-nominal shear capacity ratio; 8) Applied flexure-nominal flexural capacity ratio; 9) CB=concrete crushing/rebar buckling, BR=rebar buckling/rupture, DC=diagonal compression, OOP=out-of-plane instability

3.1 Specimen RW2

Specimen RW2 (Thomsen IV and Wallace 1995) was a relatively slender RC wall characterized with a shear-span ratio of 3.1, axial load of 0.09$A_gf'_c$, and a low shear stress demand of 0.22$\sqrt{f'_c}$ MPa (2.7$\sqrt{f'_c}$ psi) at flexural capacity, which experienced flexural failure due to crushing/buckling at the wall boundaries. Figure 2 displays the lateral load versus top displacement and shear and flexural displacement components of the 1st story (elevation 915 mm form the base) of the specimen. Although the global load-displacement response predicted by the model is in good agreement with the experimental measurements, the shear component of the 1st story displacement is slightly overestimated by the model and the flexural component rather underestimated. The total, shear and flexural displacement profiles of the specimen are plotted in Figure 3. As can be seen in this figure, the total displacement profile of the numerical model matches well with the test measurement. The shear and flexural components, however, are rather overestimated and underestimated, respectively. The predicted contribution of shear and flexural displacements to the total top displacement of the model are compared with the ones measured in the test in Figure 4a. With a shear-span ratio of 3.0, the dominant portion of the top displacement expectedly comes from flexural displacement in both the model and test results. The overestimation of the shear displacement can be observed in this plot, too. It should be noted that the calculation of shear deformation in the analysis was based on the average shear strain (G_{xy}) of the mesh elements, while the diagonal gauges mounted on the face of the specimen are used for calculation of the shear displacement in the experiments. This difference might have some impact on the discrepancy between numerical predictions and experimental measurements.

Figure 4b displays the concrete strain measurements of Specimen RW2 at the base in comparison with the model predictions at the positive peak of some selected drift cycles applied during the test. The average concrete strains were measured by seven LVDTs over a 229 mm gage length at the base of the wall. The average concrete strain of two consecutive meshes (100x100mm) at the base is used for comparison. As shown in Figure 4b, the analysis and test results are relatively close at different drift levels and the analysis was able to predict the nonlinear strain gradient along the wall length. Structural walls generally exhibit nonlinear strain gradients at the base unless the boundary zone is affected by strain localization (Dashti et al. 2018d). At 2.0% drift level, the difference between the test and analysis is relatively large although the strain profiles follow similar pattern. This difference can be attributed to the bond-slip effect which becomes more influential at higher displacement levels and is not

4

considered in the analysis. Also, the neutral axis position, which is one of the main factors in calculating the confinement length, is well predicted by the analysis.
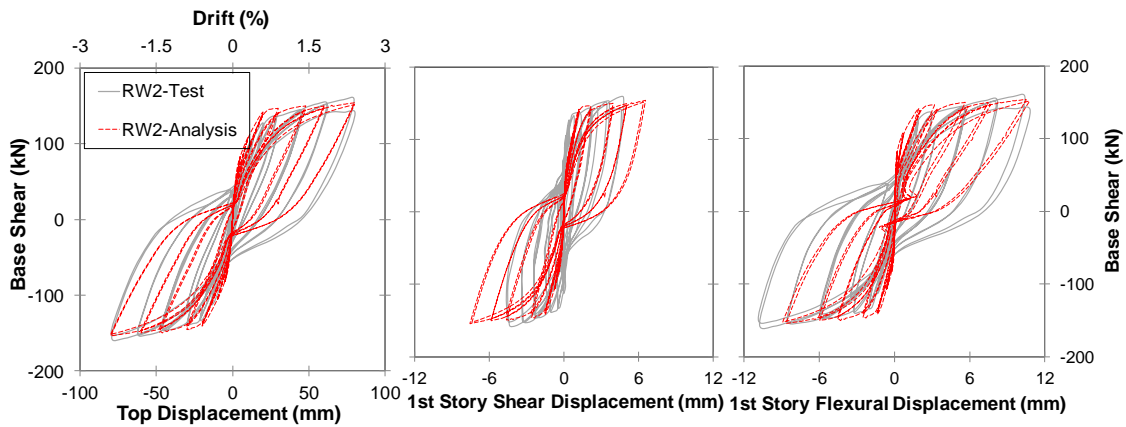

Figure 2. Lateral load vs top displacement, vs 1st story shear and 1st story flexural displacement components of Specimen RW2
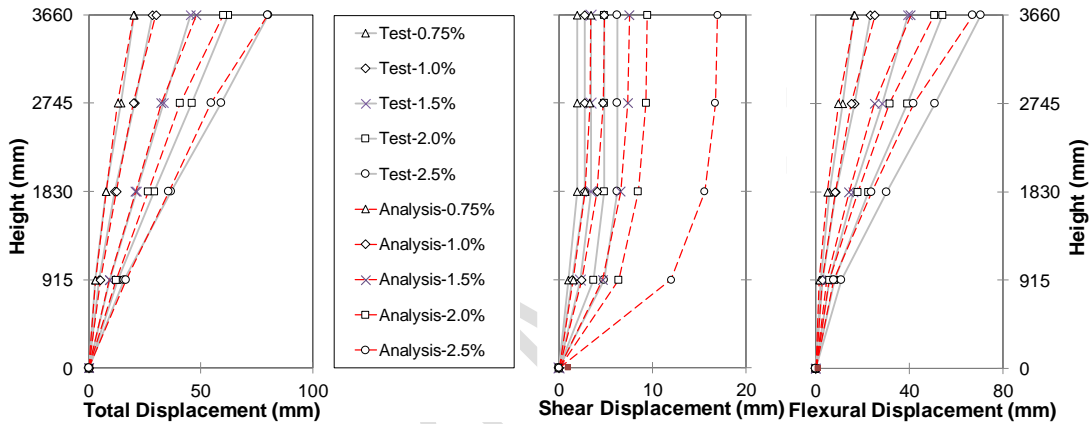

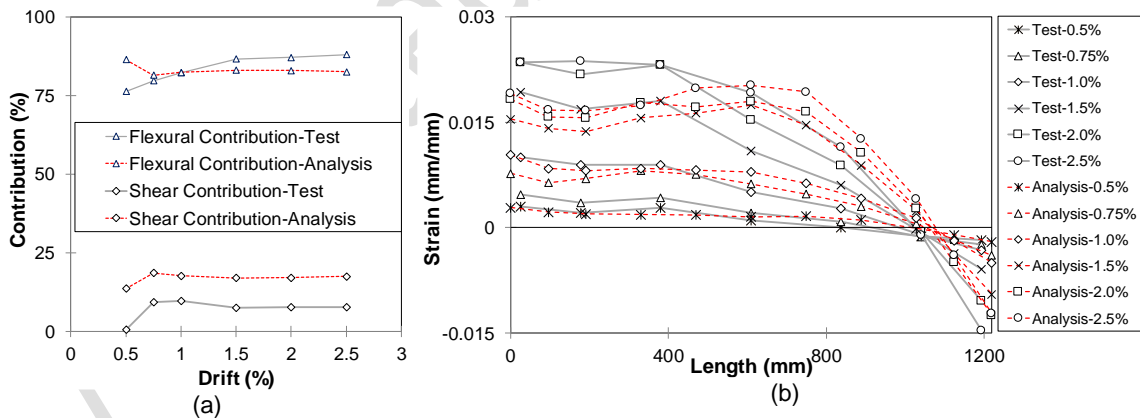**Figure 3: Displacement profiles of Specimen RW2 at positive drift levels**

Figure 4: (a) Contribution of shear and flexure to top displacement of Specimen RW2; (b) strain gradients along the length of Specimen RW2

3.2 Specimen SP4

RW-A15-P10-S78 (referred to as SP4 for brevity) (Tran and Wallace 2015) was a medium-rise RC wall with a shear-span ratio of 1.50, axial load of 0.10Agf'c, and high shear stress demand of 0.65√f'c MPa (7.8√f'c psi), which experienced significant shear-flexural interaction and diagonal compression failure. Strength loss of this specimen was initiated by concrete spalling at wall boundaries at 2.0% drift, followed by concrete crushing along diagonal compression struts at wall boundaries and rebar buckling at 3.0% drift, subsequently resulting in shear sliding along the plane adjacent to the wall-pedestal interface. Figure 5 displays the lateral load versus top displacement and top shear and flexural displacement components for Specimen SP4. As can be seen in this figure, the hysteretic response of the specimen was reasonably well-predicted by the model. However, the strength

5

degradation observed in the test could not be captured by the model which could be attributed to the fact that the bar buckling and consequently the subsequent progressive concrete crushing could not be represented in the analysis. The analysis was therefore continued up to 4.0% drift and the results exhibited noticeable strength degradation. The analysis results showed diagonal compression stress exceeding the maximum strength capacity of the confined boundary zone and unconfined panel (indication of concrete crushing in these zones) at 2.0% drift followed by initiation of shear sliding during the 2nd cycle of the 3.0% drift and at the elevation of about 150 mm from the base, which is in agreement with the experimental observations. The cyclic shear and flexural displacement components show a reasonable match with the test results (Figure 5); nonetheless, the abrupt increase of the shear displacement during the 2nd cycle of the 3.0% drift was not predicted. However, comparison of the shear hysteretic loops within a specific drift level (notably in 3.0% and 4.0% drift levels) indicate that cyclic degradation was represented in the analysis (the last 3 cycles in the shear hysteretic curve correspond to the 4.0% drift and the preceding 3 cycles correspond to the 3.0% drift).
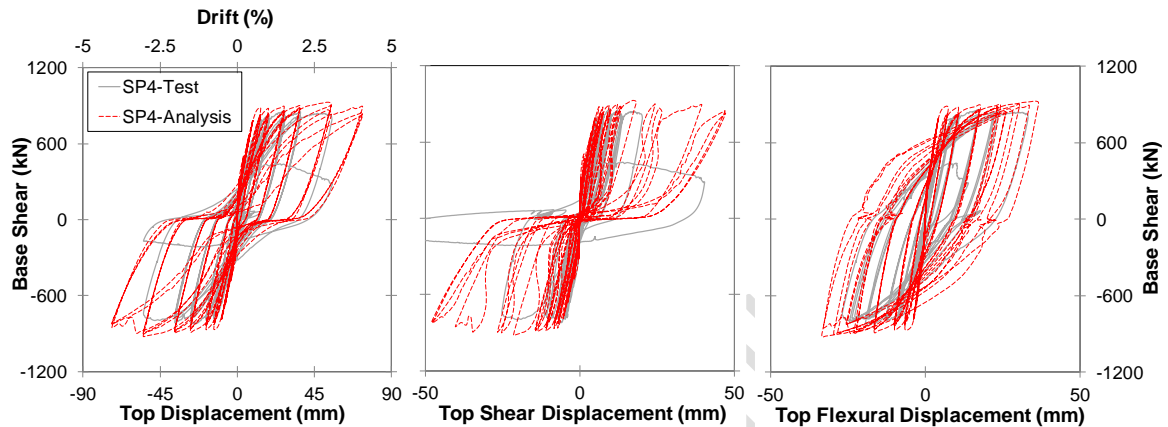

Figure 5. Lateral load vs top total displacement, top shear and top flexural displacement components of Specimen Sp4

The contribution of shear and flexural displacements to the top displacement at different stages of loading, shown in Figure 6a, indicates the increase of shear displacement in the test starting from the 2.0% drift. The contribution of shear displacement in analysis increased rapidly from 3.0% to 4.0% drift. It should be noted that the contribution plot represents the values of the 1st cycle at each drift level and, as shown Figure 5, there was a significant increase between the 1st and 2nd cycle of the 3.0% drift in terms of the predicted shear displacement. The strain gradient of the model is also in good agreement with the test measurements (Figure 6b). The experimental total displacement profile as well as the shear and flexural displacement profiles are compared with the model results in Figure 7. While the predicted total displacement profile matches quite well with the test results, the shear displacement distribution was slightly overestimated at earlier stages of loading (i.e., underestimation of flexural displacement) and somewhat underestimated at 3.0% drift.
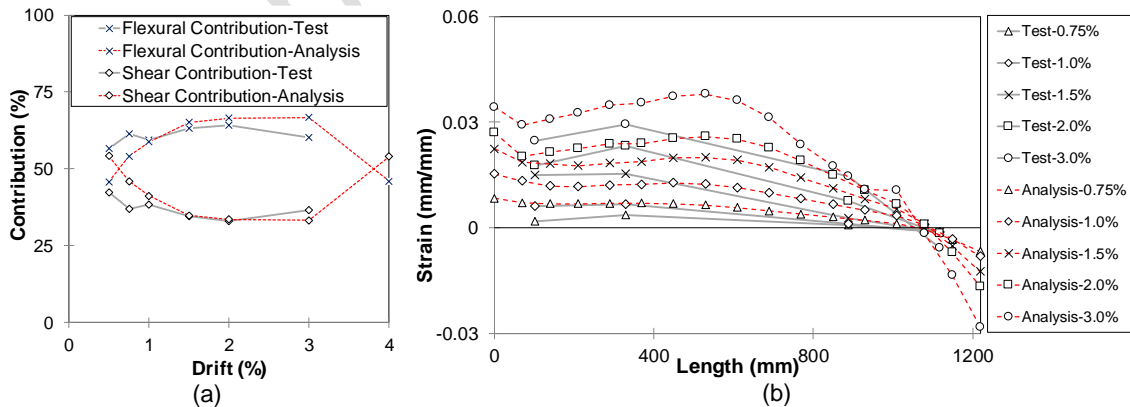

Figure 6. (a) Contribution of shear and flexure to top displacement of Specimen SP4; (b) strain gradients along the length of Specimen SP4

The axial growth prediction of the model is compared with the test measurements in Figure 8a. The experimental failure at 3.0% drift was associated with a significant drop in the axial growth curve while the numerical model although loaded up to 4.0% drift did not exhibit this significant degradation. As also noted above, bar buckling and consequently its key effect on the progressive concrete crushing was not represented in the analysis and is more likely to be the reason for this difference. The final damage state of the specimen is compared with the principal plastic strain (E1) distribution of the model at 3.0% and 4.0% drift levels. This type of damage

throughout the length of the specimen resulted in sliding shear at 3.0% drift. In the analysis, the damage extended along almost the whole length, triggered sliding shear starting from the 2nd cycle of the 3.0% drift, which increased significantly in the subsequent cycles.
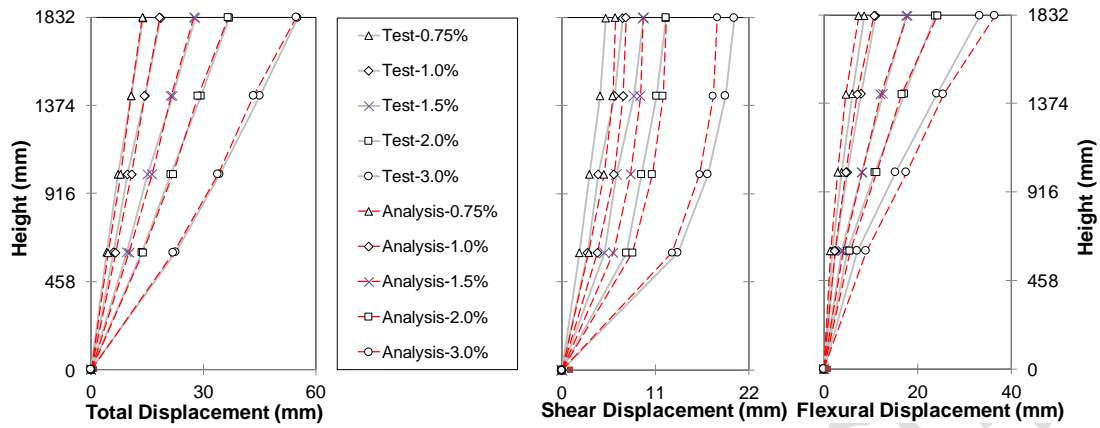

Figure 7: (a) Displacement profiles of Specimen SP4 at positive drift levels
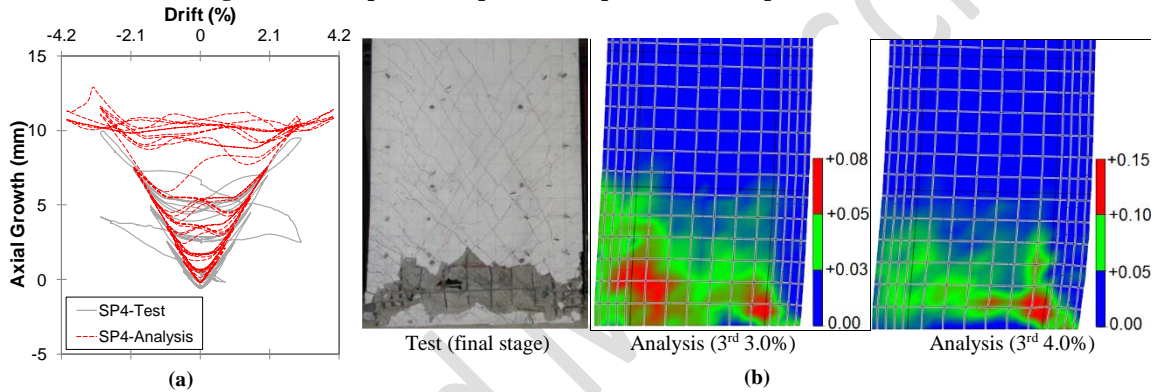

Figure 8: (a) Axial growth; (b) comparison of final damage state of Specimen SP4 with the Principal Plastic Strain-E1 predicted by the model

3.3 Specimens R2, WSH6 and S6

R2 (Oesterle et al. 1976), was a relatively slender RC wall, with an aspect ratio of 2.35, no axial load, and a low shear stress demand of $0.17\sqrt{f'c}$ MPa $(2.1\sqrt{f'c}$ psi). This specimen started to exhibit out-of-plane deformation after being exposed to three 1.7% drift cycles. The maximum value of this initial out-of-plane displacement, which was measured at a point 1.1 m above the base, was 6.4 mm. Although this out-of-plane deformation progressed further with each cycle, the load carrying capacity of the wall remained stable. The test was stopped after the 2nd cycle of the 2.2% drift, during which the maximum out-of-plane movement reached 76.2 mm, and a lateral support was provided at the level of 1.1 m. A large out-of-plane deformation was observed within the lower 1.1 m during the 2nd 2.8% drift cycle accompanied by a reduction in the load carrying capacity by about 20%. Several bars fractured during the 1st cycle of the 3.3% drift and the out-of-plane displacement progressed further. The load carrying capacity continued to decrease during the 2nd and 3rd cycles of the 3.3% drift along with considerable crushing and loss of concrete. Figure 9a compares the lateral load-top displacement response predicted by the model with the test measurements.

Out-of-plane instability of the wall was successfully predicted by the model. Progression of this failure in the left boundary zone, which was subjected to compression during the negative displacements, is also shown in Figure 9a. Out-of-plane displacement started in the analysis during the 1.7% cycle at a point 1.3m above the base and recovered almost fully. During the subsequent cycles, however, the out-of-plane displacement, did not recover and resulted in instability of the model during the 2nd 2.8% drift cycle. It should be noted the out-of-plane support provided in the test during the 2nd 2.2% cycle was not represented in the analysis which could be one of the reasons the instability occurred earlier in the analysis. As can be seen in Figure 9a, similar to the test observation, the evolution of out-of-plane deformation did not result in any strength degradation until the stage when relatively large out-of-plane deformations occurred and resulted in instability of the model. The evolution of out-of-plane instability simulated by this modeling approach is discussed in detail by Dashti et al. (2018b), and the sequence of events resulting in this failure mode is confirmed by an experimental verification Dashti et al. (2018a).

The contribution of shear and flexural displacement components to the total top displacement (Figure 9b) indicates that the shear contribution was rather underestimated in the analysis. However, as shown in this figure, the sum of flexural and shear displacement components measured in the test exceeded 100% (the total displacement) resulting in negative values of error for this specimen. Figure 9c compares the strain gradients captured by the model with the test measurements. Due to functionality limit of the strain gauges, the test data is not available for all the drift levels. The numerical prediction has a reasonable match with the experimental results particularly in terms of the elevation corresponding to significant development of plasticity.
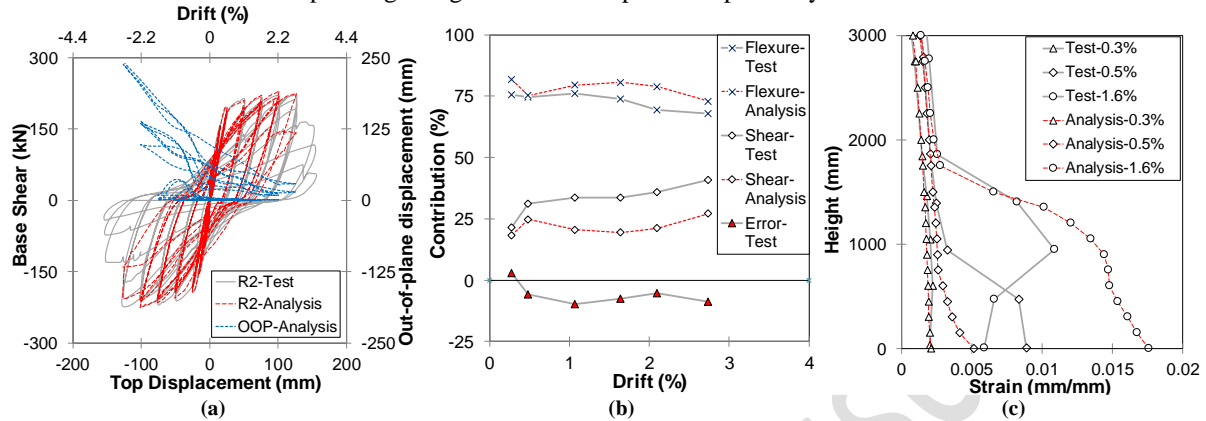
Figure 9. Numerical vs experimental results for Specimen R2: (a) Lateral load-top displacement response-OOP stands for out-of-plane displacement; (b) shear and flexural contribution; (c) strain gradients along the height

WSH6 (Dazio et al. 2009) was a moderately slender RC wall specimen with an aspect ratio of 2.02, axial load of 0.11Agf'c, and low shear stress demand of 0.3√f'c MPa (3.6√f'c psi). Concrete cover spalling started at a drift of 0.57%, the onset of buckling occurred at drift of 1.70%, while the sudden drop of wall lateral capacity occurred at drift of approximately 2.0% due to crushing of the compression zone caused by fracture of a number of confining hoops and buckling of the longitudinal boundary reinforcement.

Figure 10 compares the numerical predictions with experimental measurements in terms of lateral load vs top displacement, contribution of shear and flexural displacements to the top displacement and strain gradients along the height of the wall. The numerical load-displacement plot indicates significant pinching as compared to the experimental curve. The contribution of shear and flexural displacement components to the top displacement at different stages of loading indicates the overestimation of shear displacement by the analysis, which could be the reason for a more pinched load-displacement curve in the analysis. However, it is noteworthy that the contribution of shear and flexural components add up to 100% in the analysis, while the experimental measurements showed that the sum of calculated shear and flexural displacement components was slightly different from the total displacement (Dazio et al. 2009). The error calculated in the test is also plotted in Figure 10b. The positive values of the error show that the sum of the calculated displacement components was less than the total measured top displacement. The vertical tensile and compressive strain gradients corresponding to different drift levels are indicated in Figure 10c. While the numerical calculations match well with the test measurements up to 1.4% drift level, the compressive strain values are higher in the test at 1.70% drift. This discrepancy could be attributed to the effect of bar buckling that was initiated at this drift level in the test and was not represented in the analysis.
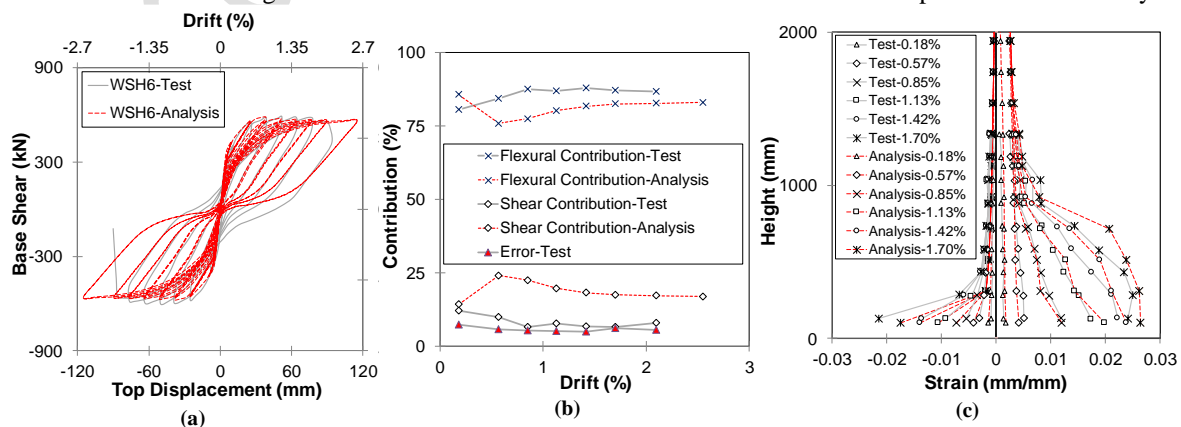
Figure 10. Numerical vs experimental results for Specimen WSH6: (a) Lateral load-top displacement response; (b) shear and flexural contribution; (c) strain gradients along the height

8

S6 (Vallenas et al. 1979) was a moderately slender RC wall with a shear-span ratio of 1.60, axial load of 0.06Agf'c, and a relatively large shear stress demand of 0.53√f'c MPa (6.4√f'c, psi). Failure of this specimen was triggered by the spalling of concrete cover on only one side of the boundary element, which resulted in out-of-plane buckling of the boundary element after spalling of the concrete cover at a story drift of 1.93%. According to the buckling photos provided in the test report, unlike the instability of Specimen R2, this buckling was mainly localized at the base where the asymmetric spalling of cover concrete could have played a triggering role. It should be noted that the specimen was tested in a horizontal position; therefore, the wall weight could have acted as a minor out-of-plane load, which could affect the wall symmetry and result in a progressive eccentricity, particularly when the wall went beyond cracking and reinforcement yielding. In order to consider this effect in the analysis, the model was subjected to an out-of-plane pressure equivalent to the wall weight. This pressure resulted in minor uniform out-of-plane displacements throughout the whole model, which became relatively large at the tensile boundary zone as all reinforcement in this region yielded. Thereafter, the out-of-plane displacement almost remained constant until the load was reversed, producing compressive stresses in the previously tensile boundary region. This compression boundary element, which was previously subjected to large tensile strains, exhibited an increased out-of-plane deformation. This out-of-plane deformation completely recovered when the model reached the peak displacement in the reverse direction. However, the instability observed in the test was not captured by the model.

Based on the difference among the types of instabilities observed in structural walls, Dashti et al. (2018e) classified the out-of-plane instability failure into local and global failure patterns. The local instability implies to the one occurring as a result of localized failures at the wall base (e.g., concrete crushing, bar buckling, etc) with the maximum out-of-plane displacement mainly at this region. The global failure refers to development of compression yielding in the boundary zone reinforcement along a sufficient height so as to produce out-of-plane instability during load reversal with the maximum out-of-plane displacement at a higher elevation from the base. The type of instability occurred in Specimen S6 seems to be more in compliance with the local instability failure, while the failure pattern of Specimen R2 has the properties similar to those of the global instability. The numerical model is able to predict the global out-of-plane deformation as the failure patterns such as bar fracture, bar buckling and asymmetric cover spalling at the base are not represented in the analysis.

The shear and flexure contribution plot shown in Figure 11b indicates overestimation of shear deformation in this specimen, where the positive error values signify that the sum of the shear and flexural displacement components was less than the measured top displacement. Figure 11c shows that the pinching was also overestimated in the predicted shear displacement hysteretic curve, which could also be the reason for overprediction of pinching in the load versus total displacement curve.

4. Parametric study

The numerical model could reasonably predict nonlinear response of the test specimens. As a further investigation, a parametric study is conducted on some of the parameters that logically affect the behavior of the structural walls. As noted previously, this parametric study is merely conducted for the sake of model validation, and therefore does not include a wide range of parameters with a wide spectrum of variation per parameter. For two of the specimens, Specimen RW2 and Specimen SP4 (with the highest and lowest shear-span ratios, respectively), this validation practice is conducted using more parameters compared to the other walls (i.e., Specimens R2, WSH6 and S6).
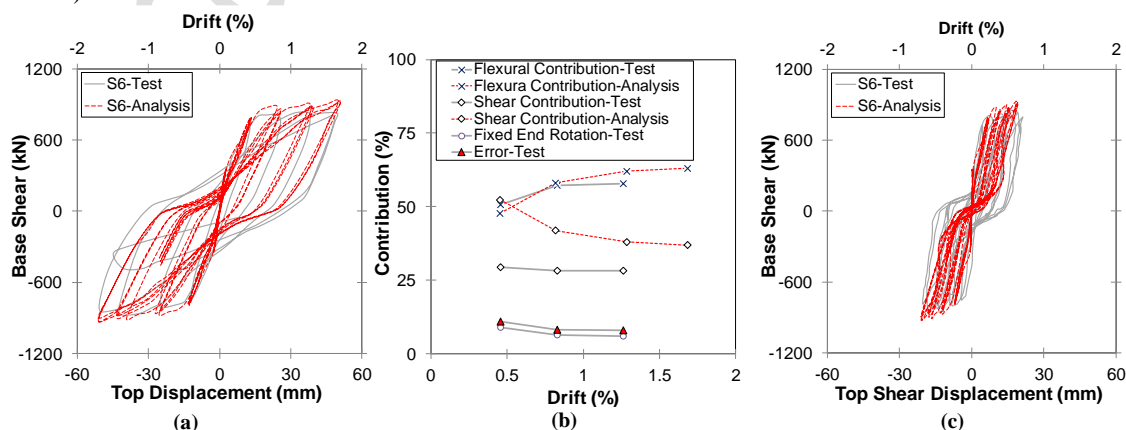

Figure 11. Numerical vs experimental results for Specimen S6: (a) Lateral load-top displacement response; (b) shear and flexural contribution; (c) lateral load-top shear displacement

9

4.1 Specimen RW2

The analysis matrix designed for parametric evaluation of the model generated for Specimen RW2 is summarized in Table 2. The effects of Shear-span ratio, axial load ratio, confinement length and total length of the wall are investigated using Models RW2-SS, RW2-A, RW2-CA and RWL, respectively. The height of RW2-SS and consequently its shear-span ratio are almost half of the ones of RW2. RW2-A is subjected to an axial load that is two times greater than the one of RW2. Under this high axial load the confinement length is reduced by 50% (denoted as RW2-CA) to highlight the importance of confinement along the neutral axis depth. RW2-L represents a wall that is higher in length compared to RW2 but has all the other features, such as shear-span ratio, confinement ratio, etc. identical to RW2. Therefore, the height and confinement length of the wall are increased so as to keep these ratios constant. These models are subjected to higher drift levels (up to 3.0%) as compared to the 2.5% drift of the test specimen to more effectively capture the trend by with the model response varies at higher drift levels. The effects of the parameters noted above on different features of wall response are investigated using lateral load vs total top displacement, vs top shear and vs top flexural displacement components (Figure 12), contribution of shear to the top displacement (Figure 24) as well as strain gradients along the length (Figure 13) and along the height of the boundary zone bar (Figure 14).

Table 2. Analysis matrix for parametric investigation of Specimen RW2

		H_w	L_w	CL	CL/L_w	t	f'_c (MPa)	f_{yBE} (MPa)	ρ_{vBE} (%)	$\rho_{h,web}/\rho_{v,web}$ (%)	M/(VL_w)	P/($A_g f'_c$)
Benchmark	RW2	3660	1219	191	0.16	102	34.0	434	2.93	0.33/0.33	3.13	0.09
1	RW2-SS	2000	1219	191	0.16	102	34.0	434	2.93	0.33/0.33	1.64	0.09
2	RW2-A	3660	1219	191	0.16	102	34.0	434	2.93	0.33/0.33	3.13	0.18
3	RW2-C-A	3660	1219	96	0.08	102	34.0	434	2.93	0.33/0.33	3.13	0.18
4	RW2-L	6125	2040	320	0.16	102	34.0	434	2.93	0.33/0.33	3.13	0.09

$\rho_{v,WEB} = 2A_{s,WEB}/(t.d)$

$\rho_{vBE} = \Sigma A_{s,BE}/(t.CL)$

To facilitate comparison between the effects of the parameters mentioned above on the cyclic response prediction of the model, the lateral load is normalized by the shear force corresponding to the nominal flexural capacity of the section, V at M_n ($\varepsilon_c = 0.003$). This shear force is denoted by V_n with the values provided for each model in Figure 12. As shown in Figure 12, the decrease in flexural demand by reducing the shear-span ratio by 45% (RW2-SS) resulted in higher shear for a given drift level (V_n) generating lower flexural displacements and larger shear deformations throughout the loading. The increase in axial load by 100% resulted in significantly pinched behavior in the hysteretic loops and understandably higher shear demand (by 25%). Under this relatively high axial load ratio, the decrease in confinement length by 50% (RW2-CA) had an adverse effect on the deformation capacity and induced an abrupt strength degradation starting from 1.0% drift level (Figure 12) and failure of the specimen at 2.0% drift level. A noticeably large increase of shear deformation during the strength degradation and failure of the model can be observed in Figure 12. The confinement length can therefore be considered as a parameter affecting the progression of concrete crushing at the base of structural walls. Dashti et al. (2014c) investigated the effect of confinement length on progression of monotonic response of rectangular walls. Under cyclic loading, the diagonal cracks previously formed in a direction perpendicular to the direction of the struts would deteriorate the compressive capacity of the strut because of repeated opening and closing. RW2-L represents a wall that is 67% (i.e., with higher length to thickness ratio) as compared to RW2 and has the same shear-span ratio. It should be noted that the confinement length to the total length was kept constant (the confinement length was increased). This increase in length would obviously increase the lever arm for the flexural capacity inducing higher shear demand (Figure 12).
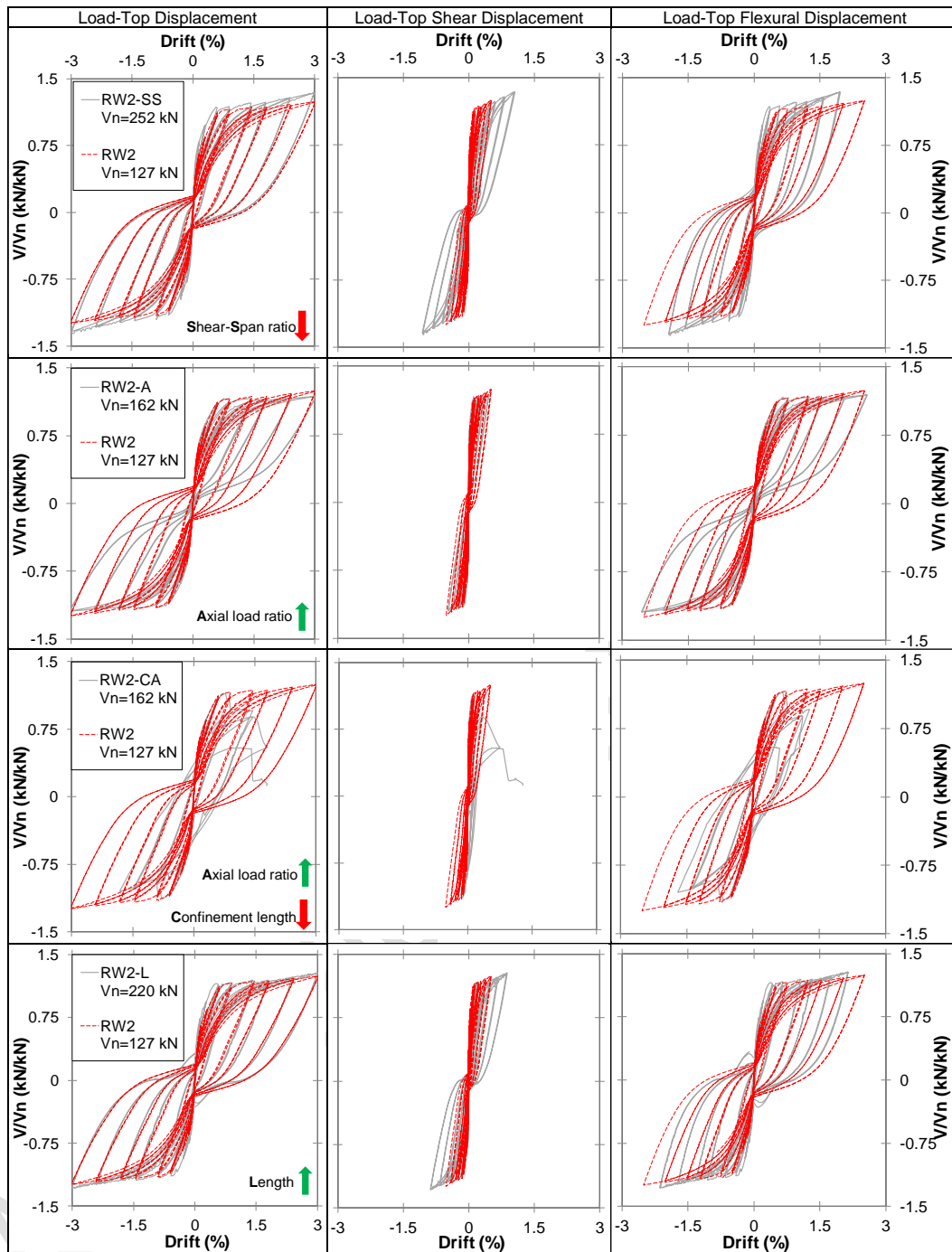
Figure 12. Lateral load vs top total displacement, vs top shear and top flexural displacement components of the parametric models for Specimen RW2

The strain gradients across the length and height of the wall would provide a better insight into the change of response and failure patterns induced by variation of different parameters. The strain profiles along the length of the wall and at the base show greater tensile and compressive strains for the lower shear-span ratio (RW2-SS compared to RW2) (Figure 13), while the strain gradients along the height indicates distribution of high tensile strains along lower elevations in the low shear-span ratio (Figure 14). The neutral axis position at the base, however, is almost constant. The increase of axial load (RW2-A) changed this neutral axis position by inducing higher compressive strains but did not have a big effect on the tension strain profile along the length. As for the tensile strain gradient along the height, the increase of axial load generated lower tensile strains at higher elevations, resulting in smaller plastic hinge length. With this noticeable increase of the neutral axis depth, the reduction of the confinement length (RW2-CA) could easily trigger crushing of the unconfined concrete and further variation of the neutral axis position to compensate for this loss of strength. This increase of the neutral

axis depth with increase in drift level resulted in lower tensile strains along the height of the wall boundary region during the 1.0% and 1.5% drift cycles as compared to RW2. Failure of the model at 2.0% drift can also be observed in the corresponding strain profile along the wall length.

The increase in the length of the wall (RW2-L) resulted in development of larger tensile and compressive strains at the base region (Figure 13). Note that the vertical strain is plotted against the normalized length. The increase in the compressive strains at the base was predicted to be significantly larger compared to tensile ones, which is apparently because of the nonlinearity of strain gradients along the wall length. While the tensile strain profile along the height (Figure 14) shows the same trend at lower elevations (i.e., the tensile strain did not increase in proportion to the increase in length), much larger tensile strains were developed at higher elevations. This figure shows that the plastic hinge length has increased with roughly the same proportion as the increase in wall length, which is in line with the equations proposed in literature for estimation of the plastic hinge length.

Figure 15a displays the axial growth plot for RW2-L compared to the one of RW2. This plot shows that although the increase in length for a constant shear-span ratio did not significantly increase the tensile strains at the base, the ratio of increase in the total elongation (axial growth) of the wall was much larger than the ratio of increase in wall length. This is due to the fact that the absolute value of the bending moment was increased to keep the shear-span ratio constant and the large tensile strains (as discussed above) was therefore distributed along a higher elevation. This discrepancy between RW2 and RW2-L in terms of the axial growth is in agreement with the difference observed in the tensile strain distribution (Figure 14). This type of strain distribution along the height of the boundary region provided ideal situation for the longitudinal bars to yield in compression along a decent height during reloading in the opposite direction prior to crack closure. Out-of-plane deformation was therefore developed in the numerical model during the 2.5% and 3.0% cycles. The out-of-plane displacement history of RW2-L (west boundary region) is plotted in Figure 15a, and the deformation pattern of RW2-L corresponding to the peak out-of-plane displacement during the 2nd 3.0% drift cycle is depicted in Figure 15b.
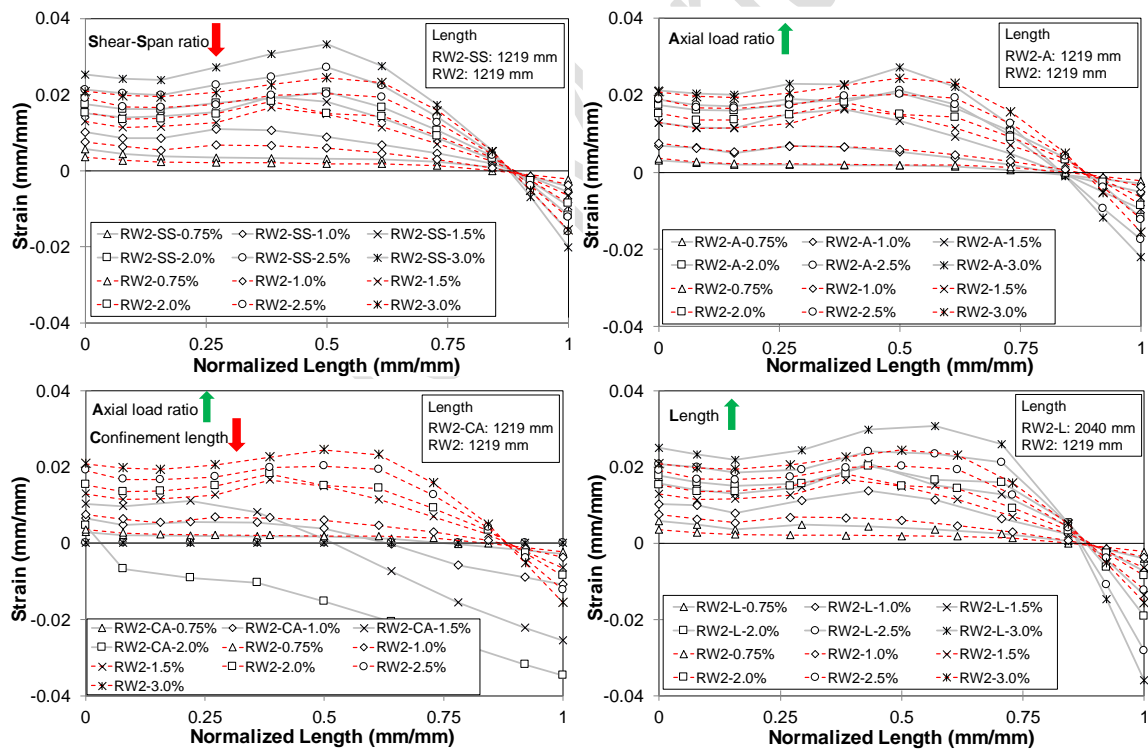

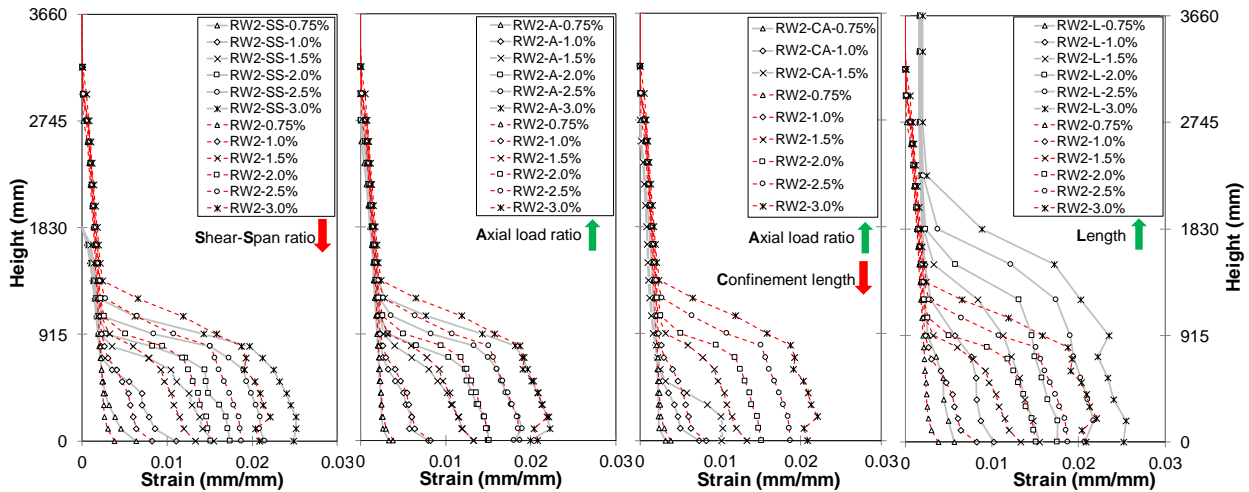**Figure 13. Strain gradients along the length of the parametric models for Specimen RW2**

Figure 14. Tensile strain gradients along the height of the parametric models for Specimen RW2
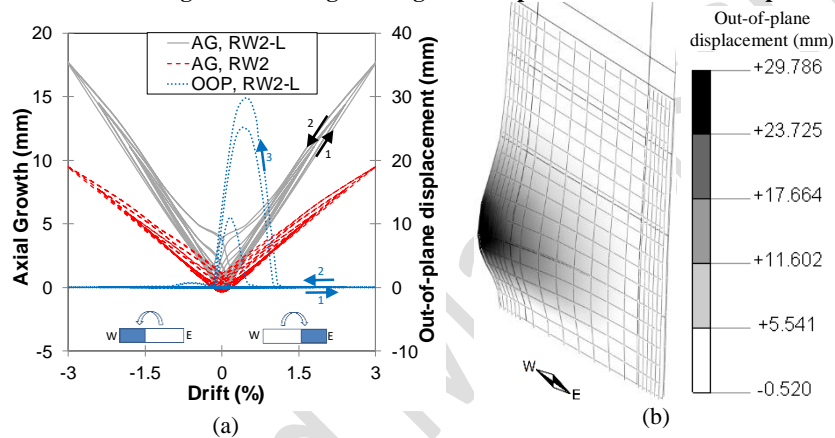

Figure 15: (a) Axial growth (AG) of RW2-L compared to RW2 and maximum out-of-plane displacement (OOP) history of RW2-L (west boundary); (b) out-of-plane displacement profile of RW2-L during the 2nd 3.0% drift cycle

4.2 Specimen SP4

The analysis matrix designed for parametric evaluation of the numerical model of Specimen SP4 is summarized in Table 3. The shear-span ratio, axial load ratio and the horizontal reinforcement ratio are considered as the variables in this parametric study. The shear-span ratio of the benchmark specimen (SP4) is 1.5, and its response is consequently affected by shear deformation. Therefore, the parameters are chosen such that they induce variation of shear demand and capacity on the model. SP4-SS1 and SP4-SS1 represent lower (0.75) and higher (3.0) shear-span ratios, respectively. SP4-A was subjected to an axial load ratio two times greater than the one applied to SP4. The ratio of the horizontal reinforcement in SP4-HRe was half of the one in SP4.

Table 3. Analysis matrix for parametric investigation of Specimen SP4

		H_w	L_w	CL	CL/ L_w	t	f'_c (MPa)	f_{yBE} (MPa)	ρ_{vBE} (%)	$\rho_{h,web}$/ $\rho_{v,web}$ (%)	M/(VL$_w$)	P/(A$_g$f$_c$)	
Benchmark	SP4	1829	1219	229	0.19	152.4	55.8	477	6.06	0.73/0.73	1.5	0.1	
1	SP4-SS1	915	1219	229	0.19	152.4	55.8	477	6.06	0.73/0.73	0.75	0.1	
2	SP4-SS2	3658	1219	229	0.19	152.4	55.8	477	6.06	0.73/0.73	3.0	0.1	
3	SP4-A	1829	1219	229	0.19	152.4	55.8	477	6.06	0.73/0.73	1.5	0.2	
4	SP4-HRe	1829	1219	229	0.19	152.4	55.8	477	6.06	0.37/0.73	1.5	0.1	

The lateral load versus top displacement as well as the top shear and flexural displacement components of the parametric models for Specimen SP4 are shown in Figure 16. SP4-SS1 was a squat wall with a shear-span ratio half of that of SP4. The shear demand was therefore increased by 100% resulting in two times greater shear stresses and shear failure of the model at 1.5% drift. The lateral load vs top shear and top flexural displacement plots (Figure 16) show a significant increase in the shear deformation and accordingly a remarkable decrease of the flexural deformation at different stages of loading. The contribution of shear to the top displacement of the model was therefore significantly greater than the one in SP4. On the other hand, the increase of shear-span ratio

13

(i.e., SP4-SS2) resulted in a flexure dominated response (as indicated by the hysteretic response plots shown in Figure 16). The shear demand was therefore decreased dramatically and so was the shear deformation. The increase of axial load (SP4-A) induced an evident strength degradation in the hysteretic curves shown in Figure 16. The decrease of the horizontal reinforcement ratio, SP4-HRe, did expectedly cause more involvement of shear displacement and consequently more pinched load-displacement curve.
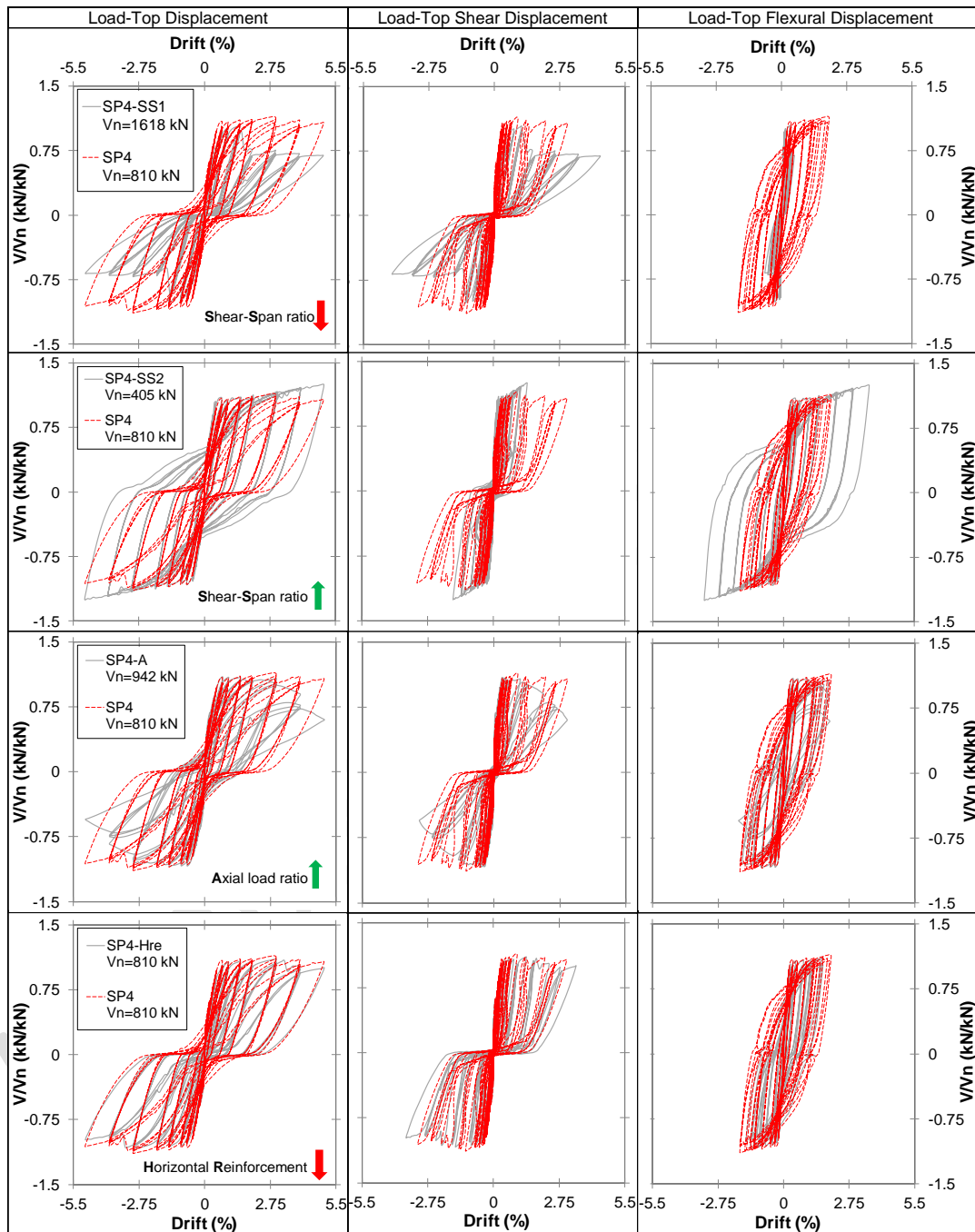

Figure 16. Lateral load vs top total displacement, vs top shear and top flexural displacement components of the parametric models for Specimen SP4

The tensile strain profiles along the boundary region height of the parametric models of Specimen SP4 are presented in Figure 17. SP4-SS1 did not have much flexural deformation and not much tensile strain was therefore developed along the height of the model. Also, the strain gradient did not change from 1.5% onwards, when the drop of strength due to shear failure occurred. SP4-SS2, however, developed large tensile strains particularly at higher elevations as compared to SP4, indicating variation of the plastic hinge length due to the increase of shear-span ratio. The increase of axial load, SP4-A, prevented development of strains above a specific level, thereby limiting the plastic hinge length to a lower value as compared to SP4. The decrease of horizontal reinforcement

14

ratio changed the strain gradient pattern in the sense that the strains followed a more uniform pattern along the height of the plastic hinge region rather than increasing linearly towards the base. This might be due to development of wide diagonal cracks throughout the length of the model generating wider cracks at higher elevations of the boundary regions.

The axial growth curves of the parametric models for Specimen SP4 are shown in Figure 18. The degradation stages of SP4-SS1 and SP4-A can be evidently observed in these plots as diagonal compression was a dominant failure in these models. However, diagonal tension was more dominant in SP4-HRe and not a big variation is observed in its axial growth plot compared to the benchmark model (SP4).
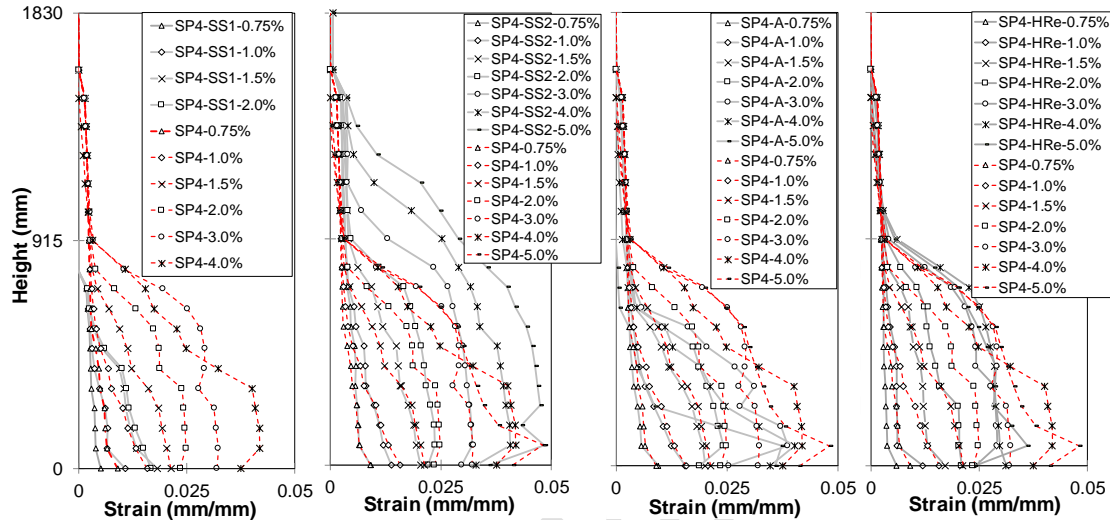

Figure 17. Tensile strain gradients along the height of the parametric models for Specimen SP4
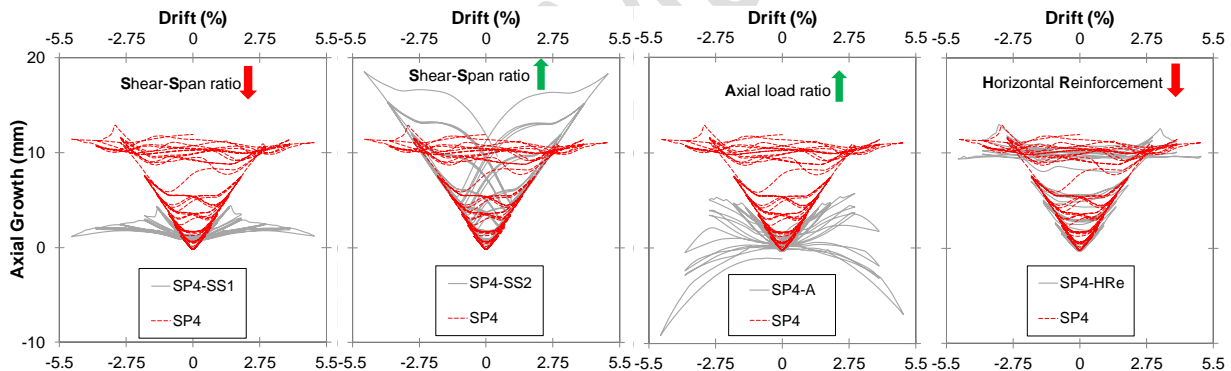

Figure 18. Axial growth of the parametric models for Specimen SP4

Figure 19 illustrates distribution of the minimum principal stress (S3) at different stages of loading for the parametric models of SP4. The intensity and direction of the stresses are shown using vectors. These contours indicate the load transfer path and participation of the panel and boundary region in load-carrying capacity of the wall. Along with these contours, distribution of the corresponding total principal strain (E1) is indicated for the models in Figure 20, which provides information on the areas where the maximum crack opening (tensile damage) is concentrated. These areas have marginal contributions to the load-carrying of the models and the values of S3 are noticeably small in these regions.

The benchmark specimen (SP4) had decent amount of contributions coming from both boundary zones (representing flexure) and the panel zone (representing shear) at 0.75% and 1.5% drift levels with high compressive stresses concentrated at the base of the unconfined panel region and confined boundary region. The development of concrete crushing in these regions at 2.0% and 3.0% drift levels, particularly in the unconfined panel region, resulted in gradual elimination of S3 vectors from these areas and their development in the upper and lower zones of the damaged area. This phenomenon resulted in higher shear displacements and consequently larger participation of the panel region in the mechanism. Evolution of the damaged zone during the 2.0% and 3.0% drift cycles led to extension of concrete crushing along the whole length and initiation of sliding shear at an elevation of about 150 mm from the base. This damage concentration and sliding is compared with the test observation in Figure 8, and the E1 contours presented in Figure 20 are in line with this mechanism.
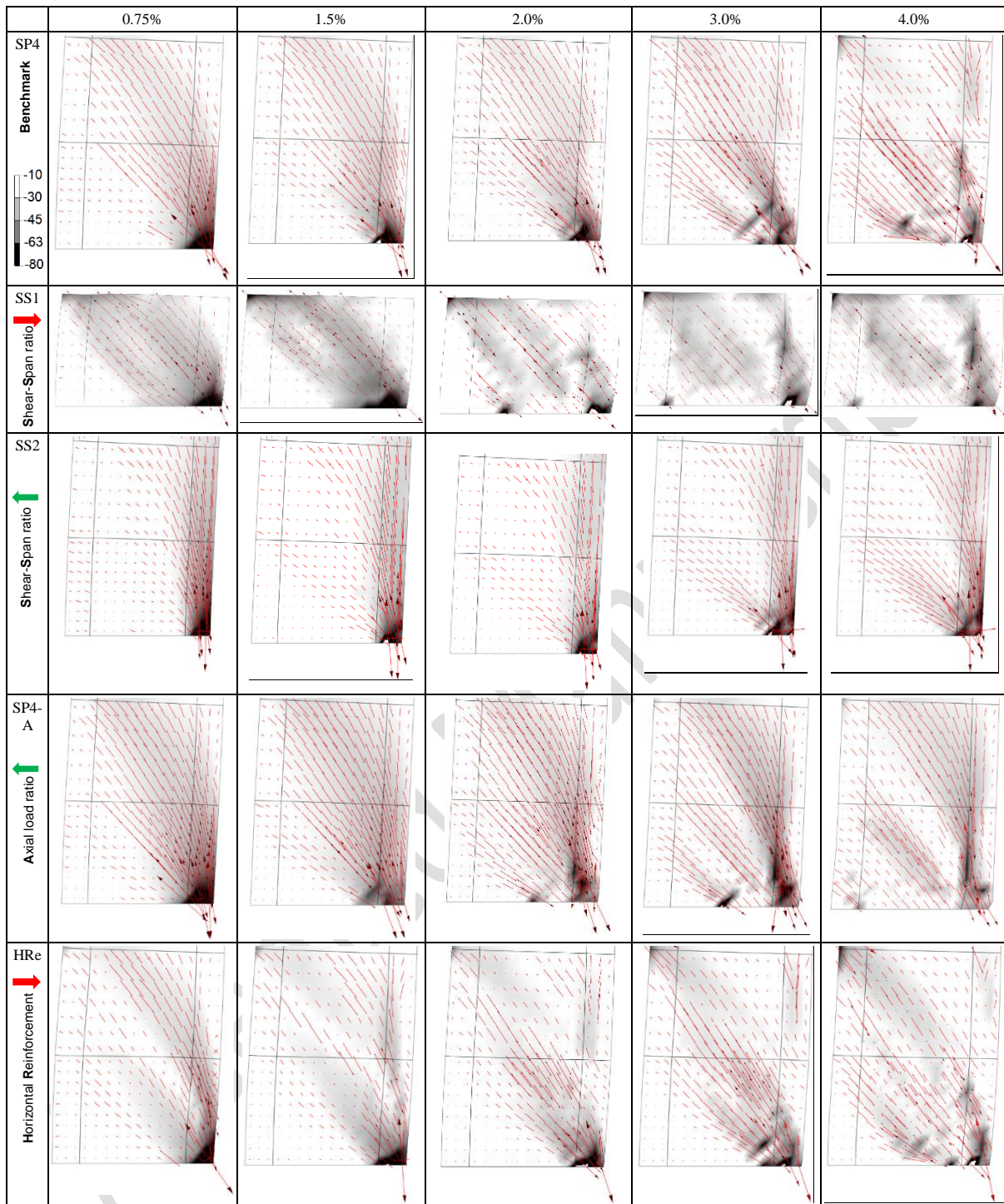
15

Figure 19. Distribution of the minimum principal stress (S3, MPa) at different stages of loading-Parametric models of Specimen SP4

The squat model (SP4-SS1) had about two times larger shear stresses which resulted in development of wide diagonal tension cracks at earlier stages followed by concrete crushing and sliding at failure. Response of the slender wall (SP4-SS2), on the contrary, was dominated by the boundary zone until 3.0% drift, where the large compressive stresses at the base penetrated into the unconfined panel and triggered increase of shear contribution during the 3.0% and 4.0% cycles. The increase of axial load (SP4-A) accelerated concrete crushing in the panel and boundary region as compared to the benchmark model. Also, the principal strain (E1) became more concentrated at the base of the model resulting in sliding to take place in this region. The model with lower horizontal reinforcement ratio had mainly diagonal cracks at 0.75% drift and the load transfer through the cracked

16

area was negligible. Evolution of flexural cracks along with these cracks can be observed throughout the subsequent loading cycles. Comparison of the E1 contours for this model with the ones of the benchmark model (SP4) indicates the increased participation of shear in the failure mechanism.
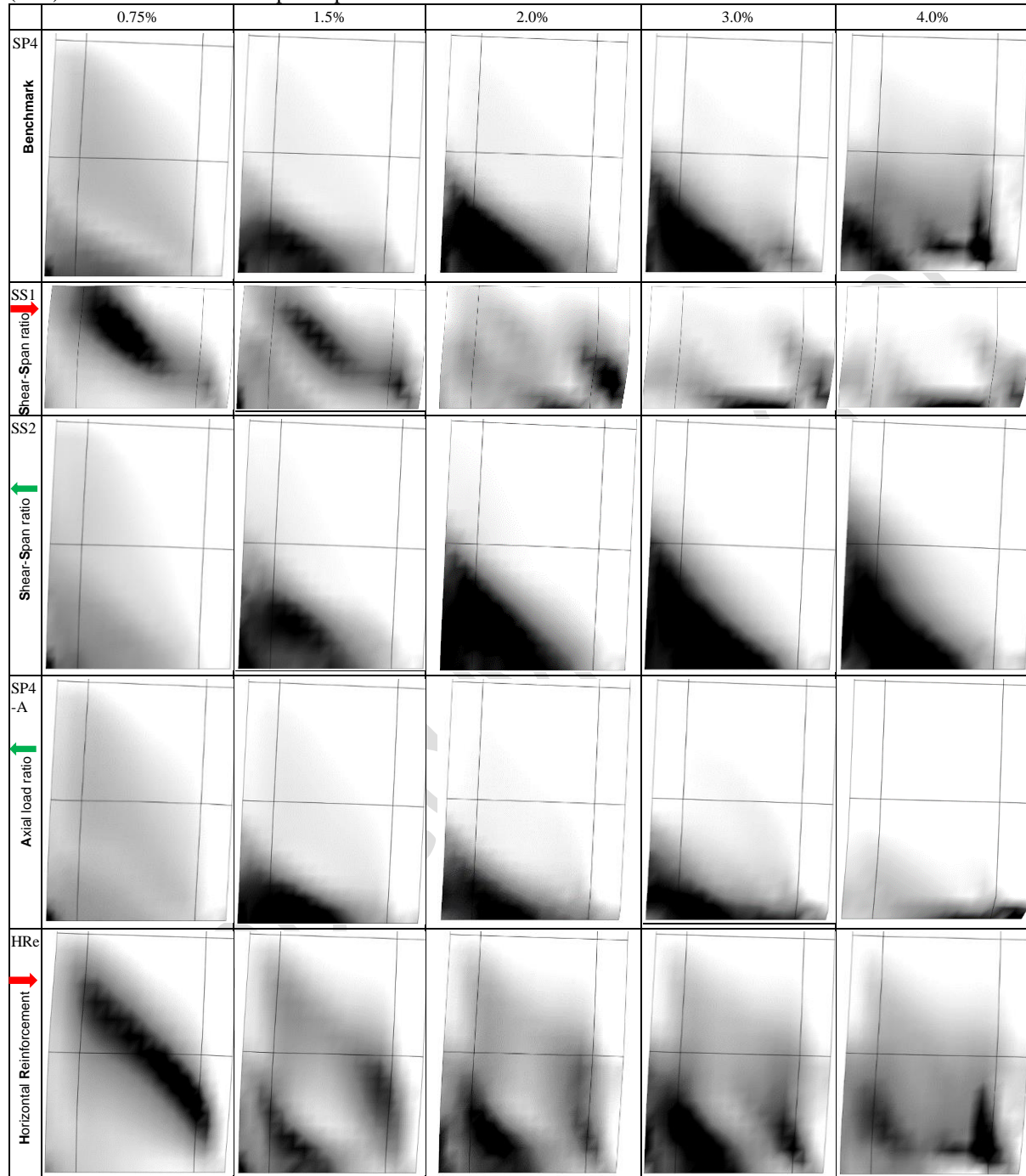

Figure 20. Distribution of the total principal strain (E1) at different stages of loading-Parametric models of Specimen SP4

4.3 Specimens R2, WSH6, S6

The parametric verification of the models for Specimens R2, WSH6 and S6 is conducted using one parameter per specimen for the sake of brevity. The parametric models for these specimens are presented in Table 4.

As elaborated in Section 3.3, the numerical model could simulate the out-of-plane instability failure of Specimen R2. The unsupported height to thickness ratio is known to be one of the major parameters controlling this mode of failure. Therefore, the thickness is slightly increased in the numerical model to evaluate sensitivity of the response to this parameter. As the thickness is increased by 10 mm only, the reinforcement ratios were not significantly affected. Figure 21 compares the response of the model with increased thickness (R2-T) with the

17

benchmark model (R2). Unlike R2, the analysis of R2-T was not terminated due to instability during the 2.2% drift cycles and was continued up to the final loading stage. Figure 21b indicates that the slight increase of the wall thickness resulted in lower values of the out-of-plane displacement during all the applied drift levels. The axial growth plot, shown in Figure 21c, also shows the effect of large out-of-plane displacement on the drop of elongation in both models.

Table 4. Parametric models for Specimens R2, WSH6 and S6

		H_w	L_w	CL	CL/l	t	f'_c (MPa)	f_{yBE} (MPa)	ρ_{vBE} (%)	$\rho_{h,web}/\rho_{v,web}$ (%)	$M/(VL_w)$	$P/(A_gf_c)$
Benchmark	R2	4572	1905	187.3	0.10	101.6	46.4	450	4.00	0.31/0.25	2.40	0.00
1	R2-T	4572	1905	187.3	0.10	11.6	46.4	450	4.00	0.31/0.25	2.40	0.00
Benchmark	WSH6	4520	2000	385	0.19	150	45.6	576	1.54	0.25/0.54	2.26	0.11
1	WSH6- Re	4520	2000	385	0.19	150	45.6	576	4.62	0.25/0.54	2.26	0.11
Benchmark	S6	2095	2412	279	0.12	114	27.8	482	5.6	0.55/0.55	1.6	0.05
1	S6-A	2095	2412	279	0.12	114	27.8	482	5.6	0.55/0.55	1.6	0.15

$\rho_{v,WEB} = 2A_{s,WEB}/(t.d)$

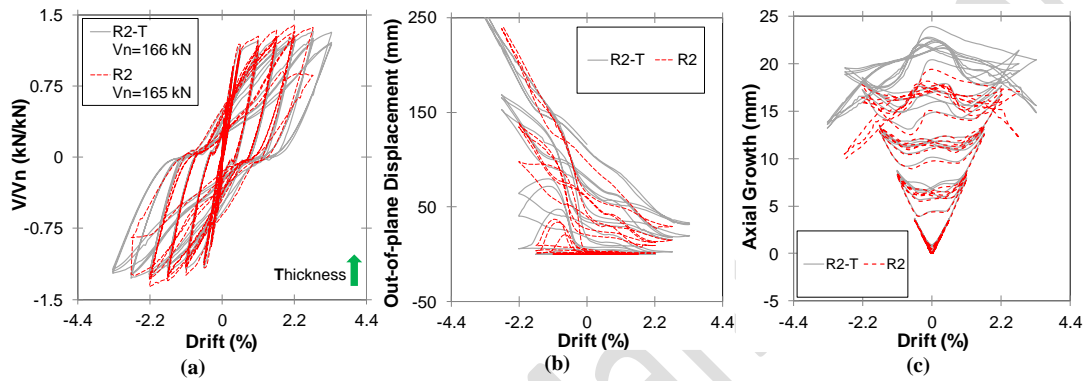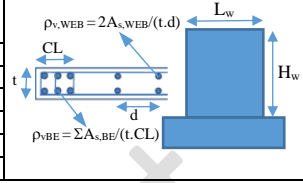$\rho_{vBE} = \Sigma A_{s,BE}/(t.CL)$

Figure 21. Parametric model results for Specimen R2: (a) Lateral load-top displacement response; (b) maximum out-of-plane displacement; (c) axial growth

WSH6 had a low reinforcement ratio in the boundary regions and was predicted to have a rather pinched response. The reinforcement content was therefore doubled in WSH6-Re which understandably resulted in higher flexural capacity and yield drift (Figure 22a). The shear demand was therefore increased significantly leading to noticeable increase in the shear contribution plot as compared to that of the benchmark model (Figure 22b). The tensile strain gradient along the boundary region height (Figure 22c) was also affected and lower vertical strains were developed in the extreme end boundary region longitudinal reinforcement.

The numerical model of Specimen S6 was subjected to an axial load three times as much as the one applied in the test (denoted as S6-A). The model (S6-A) represented failure due to diagonal compression during the first 1.3% drift cycle (Figure 23a), followed by shear sliding in the subsequent cycles. The contribution plot, shown Figure 23b, displays the rapid increase of shear deformation caused by this failure pattern. The minimum principal stress distribution of S6-A is compared with the one of S6 at the 1.3% drift along with the corresponding illustrations of the total principal strain. The large compressive stresses developed in the panel under higher axial load (S6-A) resulted in evolution of concrete crushing in the panel region next to the compression boundary (the bright area that carries a negligible load). This web crushing followed by concrete crushing in the boundary region resulted in progression of shear sliding in the model. Comparison of the total principal strain contour for S6-A with the one of S6 shows initiation of this failure at 1.3% drift.
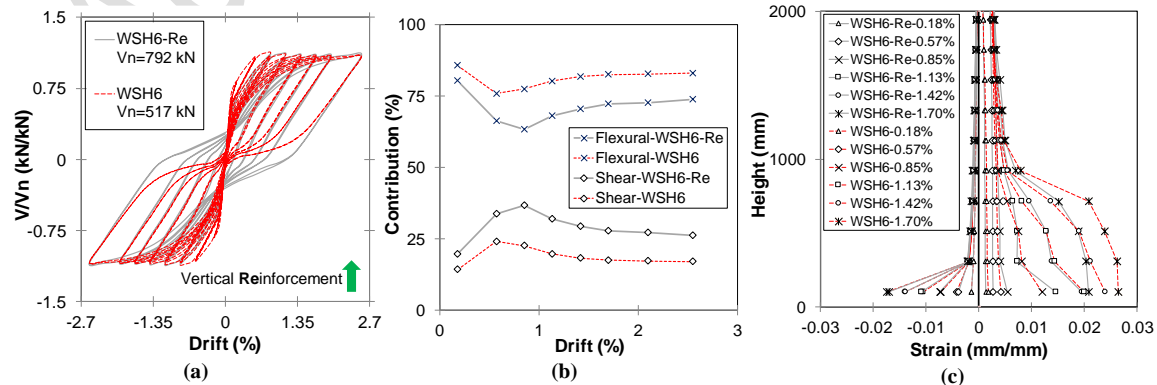

Figure 22. Parametric model results for Specimen WSH6: (a) Lateral load-top displacement response; (b) shear and flexural contribution; (c) strain gradients along the height
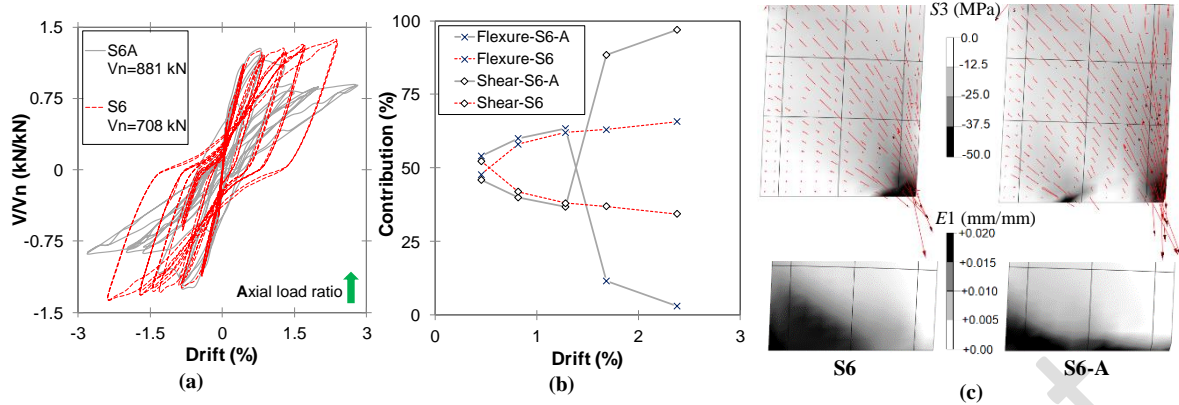
18

Figure 23. Parametric model results for Specimen S6: (a) Lateral load-top displacement response; (b) shear and flexural contribution; (c) distribution of minimum principal stress ($S3$, in MPa) and total principal strain ($E1$) at 1.3% drift

4.4 Discussion

The parametric study conducted in Sections 4.1-4.3 evaluated sensitivity of the nonlinear response of several wall specimens to variation of some parameters chosen based on their specific characteristics and observed failure patterns. The numerical model could represent the effects of these parameters on nonlinear response of the selected specimens (e.g., changing the response mode from flexure to shear and vice versa) and on progression of several shear failure patterns (including diagonal tension, diagonal compression and sliding shear) and the flexural failure modes induced by concrete crushing and out-of-plane instability. However, bar buckling as well as bar fracture and their interaction with other failure modes were not captured as these failure modes are not incorporated in the model. It is well understood that the amount of strength degradation would have been predicted more accurately if the influence of these parameters on the wall response (e.g., progressive concrete crushing induced by bar buckling) had been included in the model. However, other measures of wall response can be investigated along with the global load-displacement curves to study the effect of different parameters on development of strength degradation and subsequent failure. These measures include stress and strain contours as well as the contribution of shear and flexural displacements to the total top displacement which can serve as an indication of the dominant mode of response and the drift level corresponding to initiation of strength degradation and subsequent failure. Figure 24 presents the shear contribution plot of the parametric models generated for Specimens RW2 and SP4. The points corresponding to initiation of strength degradation in the load-displacement curves are indicated in this figure. It should be noted that the contribution plots correspond to the 1st cycle of each drift level and the cyclic degradation would obviously alter the values for the subsequent (2nd and 3rd) cycles at each drift level.

As can be seen in Figure 24a, contribution of shear displacement to the top displacement increased by 20% when the shear-span ratio of RW2 decreased by about 50%, RW2-SS, causing the same amount of decrease in the flexural displacement. Also, this contribution is not constant throughout the loading. The flexural contribution increased up to 1.5% drift and started to gradually decrease afterwards (i.e., the shear contribution started to increase after 1.5% drift). As for the increase in wall length for a constant shear-span ratio, RW2-L, the shear stress was increased leading to higher contribution of shear deformation to the total top displacement since the thickness was kept constant. The increase of axial load, RW2-A, did not have a big impact on the contribution of the shear and flexural displacements to the total top displacement, which led to minor increase of the flexural contribution and consequently slight decrease of the shear contribution. The decrease of confinement length under the increased axial load, RW2-CA, however, resulted in noticeably large increase of shear deformation and initiation of failure at 1.5% drift.

According to the contribution plots of SP4, shown in Figure 24b, reduction of the shear-span ratio from 1.5 to 0.75, SP4-SS1, resulted in dramatic increase in contribution of shear compared to that of SP4, and the shear failure of the model at 1.5% drift led to a rapid increase of the shear contribution. The decrease of the horizontal reinforcement ratio, SP4-HRe, did expectedly result in higher contribution of shear displacement. The shear contribution plot indicates steady increase of shear contribution starting at 2.0% drift as compared to the one in SP4 which initiated at 3.0% drift. The increase of axial load, SP4-A, apparently did not have a big impact on the contribution percentage of shear and flexural displacements. The increase of shear contribution, however, started at a lower drift (1.5%), when the strength degradation started to develop. Although the variation of shear contribution due to the increase of shear-span ratio from 1.5 to 3.0, SP4-SS2, was not as noticeable as the one corresponding to SP4-SS1, no abrupt increase of shear contribution was noticed in this case and the response was flexure-dominated.
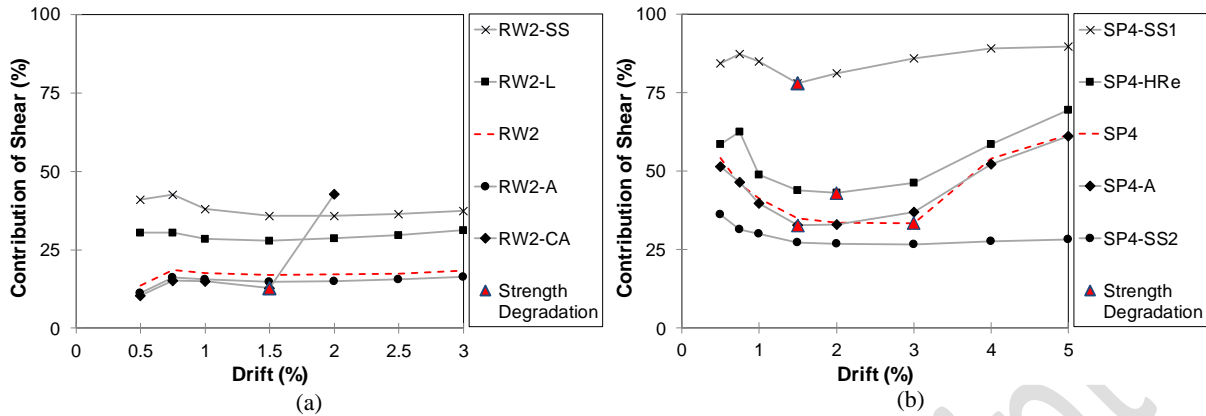
19

Figure 24. Contribution of shear displacements to the top displacement-parametric models of Specimen RW2 (a) and Specimen SP4 (b)

5. Summary and conclusions

A numerical model based on curved shell element was validated in this study using the parametric analysis approach. The sensitivity of the model response to variation of different parameters known to be influential on nonlinear response of structural walls was evaluated using test results of wall specimens that had exhibited a variety of failure models. The parameters included shear-span ratio, axial load ratio, confinement length, horizontal and vertical reinforcement ratios, thickness and length. As this study merely focused on evaluating capabilities of the model and not on parametric investigation of the nonlinear response in structural walls, the parameters noted above were changed within a limited range and using few parametric models. In addition to this sensitivity analysis, the model response was compared with the experimental measurements in terms of a wide range of response factors. This range included lateral load to total top displacement and load versus shear as well as flexural displacement components, relative contribution of shear and flexural displacement components at different stages of loading, vertical strain gradients along the length and height of the wall, axial growth, and shear, flexural as well as displacement profiles along the height of the wall. For the sake of brevity, not all these parameters were used for validation of the model prediction for all the specimens. The strengths and limitations of the model identified using the experimental and parametric verification described above are listed below:

- The lateral load versus top total displacement, versus top shear displacement, and versus top flexural displacement responses are predicted reasonably well in terms of the shape of the hysteretic curve and cyclic degradation. The initial stiffness is generally overestimated. This is particularly noticeable for the post-cracking stiffness although the cracking strength is not far-off in most cases. The peak strength in each cycle is generally overestimated. The maximum discrepancy was around 12% among the specimens used in this study. The pinching is overestimated in most cases. This could be attributed to overpredition of pinching in the shear displacement component.
- The difference between numerical and experimental results in terms of the relative contribution of flexural and shear displacement components to the total top displacement throughout loading was noticeable in some cases. The overall trend, however, is generally in line with the experimental measurements.
- Although the total displacement profile is predicted fairly accurately, the shear displacement profile indicates overestimation of shear in some cases.
- The nonlinear strain gradient along the length of the wall is well captured by the model. The strain values, however, are generally underestimated. This discrepancy could be attributed to the bond deterioration and strain penetration effects that are not represented in the analysis.
- The vertical strain gradient along the boundary region reinforcement fairly predicts the elevation of plasticity. The values of the tensile and compressive strains, however, may not be accurately calculated by the analysis due to non-representation of phenomena like bar buckling, bond deterioration, low-cycle fatigue and the resulting bar fracture.
- The failure patterns successfully predicted by the model include: i) concrete crushing in slender walls under high axial load and with low confinement; ii) global out-of-plane instability of slender walls under in-plane cyclic loading; iii) diagonal tension in shear-dominant walls (squat walls) with light horizontal reinforcement; iv) diagonal compression in shear-dominant walls (squat walls) with high shear stress; v) sliding shear preceded by development of concrete crushing along the web and boundary regions.

- The failure patterns not represented in the model include: i) bar buckling and the subsequent progressive concrete crushing; ii) bar fracture and the subsequent stress redistribution; iii) local out-of-plane instability as the secondary failure mode triggered by another (initial) type of failure, such as bar buckling, asymmetric cover spalling, concrete crushing, etc.

6. Acknowledgement

7. References

Alarcon C, Hube M, de la Llera J (2014) Effect of axial loads in the seismic behavior of reinforced concrete walls with unconfined wall boundaries Engineering Structures 73:13-23

Almeida JP, Prodan O, Tarquini D, Beyer K (2017) Influence of lap splices on the deformation capacity of RC walls. I: Database assembly, recent experimental data, and findings for model development Journal of Structural Engineering 143:04017156

Beattie GJ (2004) Design of Slender Precast Concrete Wall Panels – Experimental Testing. BRANZ Ltd, Judgeford, New Zealand, BRANZ Study Report SR 129

Belarbi A, Hsu TT (1994) Constitutive laws of concrete in tension and reinforcing bars stiffened by concrete ACI Structural Journal 91

Brueggen BL, French CE, Sritharan S (2017) T-shaped RC structural walls subjected to multidirectional loading: Test results and design recommendations Journal of Structural Engineering 143:04017040

Chang G, Mander JB (1994) Seismic energy based fatigue damage analysis of bridge columns: Part I-Evaluation of seismic capacity. National Center for Earthquake Engineering Research Buffalo, NY,

Dashti F, Dhakal RP, Pampanin S (2017) Numerical Modeling of Rectangular Reinforced Concrete Structural Walls Journal of Structural Engineering 143 doi:10.1061/(ASCE)ST.1943-541X.0001729

Dashti F, Dhakal RP, Pampanin S (2018a) Evolution of out-of-plane deformation and subsequent instability in rectangular RC walls under in-plane cyclic loading: Experimental observation Earthquake Engineering and Structural Dynamics doi:10.1002/eqe.3115

Dashti F, Dhakal R, Pampanin S (2014a) Numerical simulation of shear wall failure mechanisms. Paper presented at the 2018 NZSEE Conference, Auckland, New Zealand

Dashti F, Dhakal RP, Pampanin S (2014b) Simulation of out-of-plane instability in rectangular RC structural walls. Paper presented at the Second European Conference on Earthquake Engineering and Seismology, Istanbul, Turkey, Aug. 25-29, 2014

Dashti F (2017) Out-of-plane Instability of Rectangular Reinforced Concrete Walls Under In-plane Loading. PhD Thesis, Department of Civil and Natural Resources Engineering, University of Canterbury

Dashti F, Dhakal RP, Pampanin S (2018b) Validation of a Numerical Model for Prediction of Out-of-plane Instability in Ductile Structural Walls under Concentric In-plane Cyclic Loading Journal of Structural Engineering doi:10.1061/(ASCE)ST.1943-541X.0002013

Dashti F, Dhakal RP, Pampanin S (2018c) Blind prediction of in-plane and out-of-plane responses for a thin singly reinforced concrete flanged wall specimen Bull Earthquake Eng 16:427–458 doi:10.1007/s10518-017-0211-x

Dashti F, Dhakal RP, Pampanin S (2018d) Inelastic Strain Gradients in Reinforced Concrete Structural Walls. Paper presented at the 16th European Conference on Earthquake Engineering, Thessaloniki, Greece

Dashti F, Dhakal R, Pampanin S (2018e) Local vs Global Instability of Ductile Structural Walls. Paper presented at the 2018 NZSEE Conference, Auckland, New Zealand

Dashti F, Dhakal RP, Pampanin S (2014c) Comparative in-plane pushover response of a typical RC rectangular wall designed by different standards Earthquakes and Structures 7:667-689

Dazio A, Beyer K, Bachmann H (2009) Quasi-static cyclic tests and plastic hinge analysis of RC structural walls Engineering Structures 31:1556-1571

Dhakal RP, Maekawa K (2002b) Reinforcement stability and fracture of cover concrete in reinforced concrete members Journal of Structural Engineering 128:1253-1262

DIANA T (2011) Finite Element Analysis User's Manual - Release 9.4.4, 9.4.4 edn. TNO DIANA,

Fischinger M, Kante P, Isakovic T (2017) Shake-table response of a coupled RC wall with thin T-shaped piers Journal of Structural Engineering 143:04017004

Goodsir WJ (1985) The design of coupled frame-wall structures for seismic actions. University of Canterbury

Haro AG, Kowalsky M, Chai YH, Lucier GW (2018) Boundary Elements of Special Reinforced Concrete Walls Tested Under Different Loading Paths Earthquake Spectra 0:null doi:10.1193/081617eqs160m

Herrick CK, Kowalsky MJ (2016) Out-of-Plane Buckling of Ductile Reinforced Structural Walls due to In-Plane Loads Journal of Structural Engineering 0:04016182 doi:doi:10.1061/(ASCE)ST.1943-541X.0001660

Johnson B (2010) Anchorage detailing effects on lateral deformation components of R/C shear walls. Master Thesis, University of Minnesota

Kolozvari, K., C. A. Arteta, M. Fischinger, S. Gavridou, M. Hube, T. Isakovic, L. Lowes, K. Orakcal, J. Vásquez and J. W. Wallace (2018). "Comparative Study of State-of-the-Art Macroscopic Models for Planar Reinforced Concrete Walls." ACI Structural Journal. DOI: 10.14359/51710835.

Kolozvari, K., L. Biscombe, F. Dashti, R. Dhakal, A. Gogus, M. F. Gullu, R. Henry, L. Massone, K. Orakcal, F. Rojas, A. Shegay and J. Wallace (2019). "State-of-the-art in Nonlinear Finite Element Modeling of Planar Reinforced Concrete Walls." Engineering Structures (in press)

Kolozvari K, Wallace JW (2016) Practical nonlinear modeling of reinforced concrete structural walls Journal of Structural Engineering 142:G4016001

Lu Y, Henry RS, Gultom R, Ma QT (2016) Cyclic testing of reinforced concrete walls with distributed minimum vertical reinforcement Journal of Structural Engineering 143:04016225

Menegotto M, Pinto P Method of Analysis for Cyclically Loaded Reinforced Concrete Plane Frames Including Changes in Geometry and Non-elastic Behavior of Elements Under Combined Normal Force and Bending. In: IABSE Symposium on the Resistance and Ultimate Deformability of Structures Acted on by Well-Defined Repeated Loads, Lisbon, 1973. Association internationale des ponts et charpentes,

Mindlin RD (1951) Influence of rotary inertia and shear on flexural motions of isotropic, elastic plates J of Appl Mech 18:31-38

Oesterle R, Fiorato A, Johal L, Carpenter J, Russell H, Corley W (1976) Earthquake Resistant Structural Walls: Tests of Isolated Walls. Research and Development Construction Technology Laboratories, Portland Cement Association,

Orakcal K, Wallace JW (2006) Flexural modeling of reinforced concrete walls-experimental verification ACI Structural Journal 103

Parra PF (2016) Stability of Reinforced Concrete Wall Boundaries. University of California, Berkeley

Parra PF, Moehle JP (2017) Stability of Slender Wall Boundaries Subjected to Earthquake Loading ACI Structural Journal 114:1627-1636

Reissner E (1945) The effect of transverse shear deformation on the bending of elastic plates Journal of applied Mechanics 12:69-77

Rosso A, Almeida J, Beyer K (2015) Stability of thin reinforced concrete walls under cyclic loads: state-of-the-art and new experimental findings Bull Earthquake Eng:1-30 doi:10.1007/s10518-015-9827-x

Rosso A, Jiménez-Roa LA, de Almeida JP, Zuniga APG, Blandón CA, Bonett RL, Beyer K (2017a) Cyclic tensile-compressive tests on thin concrete boundary elements with a single layer of reinforcement prone to out-of-plane instability Bull Earthquake Eng doi:10.1007/s10518-017-0228-1

Rosso A, Jime´nez L, Almeida J, Beyer K (2017b) Experimental campaign on thin RC columns prone to out-of-plane instability: numerical simulation using shell element models. In: VIII Congreso Nacional de Ingenierı´a Sı´smica, Barranquilla, Colombia

Sanada Y, Yamamoto N, Ichinose T, Takahashi S, Tani M, Fukuyama H (2017) Flexure mechanism and deformation at bending-compression failure of RC structural walls Journal of Structural Engineering 144:04017204

Scolari M (2017) Implementation of PARC_CL 2.0 crack model for reinforced concrete members subjected to cyclic and dynamic loading. University of Parma

Shegay AV, Motter CJ, Elwood KJ, Henry RS, Lehman DE, Lowes LN (2018) Impact of Axial Load on the Seismic Response of Rectangular Walls Journal of Structural Engineering 144:04018124

Tarquini D, Almeida JP, Beyer K (2017) Influence of lap splices on the deformation capacity of RC walls. II: Shell element simulation and equivalent uniaxial model Journal of Structural Engineering 143:04017157

Terzioglu T, Orakcal K, Massone LM (2018) Cyclic lateral load behavior of squat reinforced concrete walls Engineering Structures 160:147-160

Thomsen IV JH, Wallace JW (1995) Displacement-based design of reinforced concrete structural walls: An experimental investigation of walls with rectangular and T-shaped cross-sections. Department of Civil and Environmental Engineering, Clarkson University, Potsdam, N.Y.,

Tran TA, Wallace JW (2015) Cyclic testing of moderate-aspect-ratio reinforced concrete structural walls ACI Structural Journal 112:653

Vallenas JM, Bertero VV, Popov EP (1979) Hysteretic behaviour of reinforced concrete structural walls. Earthquake Engineering Research Center, University of California, Berkeley.,

Vecchio FJ, Collins MP (1986) The modified compression-field theory for reinforced concrete elements subjected to shear ACI Journal Proceedings 83:219-231

Welt TS, Massone LM, LaFave JM, Lehman DE, McCabe SL, Polanco P (2016) Confinement behavior of rectangular reinforced concrete prisms simulating wall boundary elements Journal of Structural Engineering 143:04016204